To cite this version :

Shaolin LIU, Azita AHMADI, Victor POZZOBON, Jean LACHAUD - Multi-scale investigation of heat and momentum transfer in packed-bed TES systems up to 800 K - Applied Energy - Vol. 366, p.123285 - 2024

Multi-scale investigation of heat and momentum transfer in packed-bed TES systems up to 800 K

Shaolin Liu [a,b,*], Azita Ahmadi-Senichault [a,b], Victor Pozzobon [c], Jean Lachaud [b,d]

[a] *Arts et Métiers Institute of Technology, 33400, Talence, France*
[b] *I2M - Institute of Mechanical Engineering of Bordeaux: UMR CNRS 5295, University of Bordeaux, Arts et Métiers Institute of Technology, Hesam Université, Bordeaux INP, INRAE, 33400, Talence, France*
[c] *Université Paris-Saclay, CentraleSupélec, Laboratoire de Génie des Procédés et Matériaux, Centre Européen de Biotechnologie et de Bioéconomie (CEBB), 3 rue des Rouges Terres 51110 Pomacle, France*
[d] *Univ. Bordeaux, 33400, Talence, France*

ARTICLE INFO

ABSTRACT

With the rising cost of energy and the advancement of corporate social responsibility, there is a growing interest in addressing the challenge of recovering and storing high-temperature waste heat. Sensible heat storage in packed beds stands out as a cost-effective and seemingly straightforward solution for high-temperature Thermal Energy Storage (TES). Engineering models developed to design low-temperature TES systems were tentatively used to design this new generation of high-temperature systems. Delving into the physics of coupled heat and mass transfer reveals a lack of validation of this approach. This study seeks to establish a comprehensive bottom-up methodology - from the particle scale up to the system level - to provide informed and validated engineering models for the design of high-temperature TES systems. To achieve this goal, we developed a multi-scale numerical model to explore the physics of heat and momentum transfer in packed-bed TES systems. At the microscopic scale (pore/particle), we consider the flow of a compressible high-temperature gas between the particles, coupled to transient heat conduction within the particles, with particular attention given to incorporating accurate temperature-dependent viscosity for the gas phase and thermal conductivity and density for both solid and gas phases. At the macroscopic scale (engineering), we propose a high-temperature extension of state-of-the-art two-equation TES models. The governing equations considered are the volume-average conservation laws for gas-mass, gas-momentum and energy of both phases. The multi-scale strategy is applied to a randomly packed bed of spherical particles generated with the discrete element method (DEM) software LIGGGHTS. Numerical models for both scales were implemented in the Porous material Analysis Toolbox based on OpenFoam (PATO), which is made available in Open Source by NASA. Microscopic scale simulations were used to infer the effective parameters needed to inform the macroscopic model, namely, permeability, Forchheimer coefficient, effective thermal conductivities, and the heat transfer coefficient. The informed macroscopic model reproduces with excellent accuracy the average temperature fields of the physics-based microscopic model. Pore-scale analysis shows highly three-dimensional flow characterized by reverse flow and strong cross-flow in the packed bed system. Moreover, it indicates the coupling between temperature and velocity fields, where a nonuniform velocity field results in uneven temperature distributions across the fluid and the solid spheres within the packed bed, subsequently affecting the macroscopic heat transfer coefficient. The overall strategy is validated by comparison to available experimental data. This bottom-up methodology contributes to the understanding and opens new perspectives for a more precise design and monitoring of high-temperature TES systems.

1. Introduction

Thermal energy storage (TES) systems are receiving increased attention for the development of energy recovery technologies such as concentrated solar power (CSP) [1], geothermal energy storage [2], nuclear power plants [3], and industrial waste heat recovery [4,5]. TES systems can be classified into three types: sensible, latent, and chemical heat storage [6]. Sensible heat storage is the most developed and employed within the industry [7]. Naturally available materials

Nomenclature

Acronyms

DEM	Discrete element method
LTNE	Local thermal non-equilibrium
REV	Representative elementary volume
XCT	X-ray computed tomography

Greek symbols

β	Forchheimer coefficient, m^{-1}
μ_g	dynamic viscosity, $\mathrm{kg\,m^{-1}\,s^{-1}}$
ω	coefficient of volume expansion, $\mathrm{K^{-1}}$
ρ_i	density of the i phase, $\mathrm{kg\,m^{-3}}$
ε_i	porosity of the i-phase

Latin symbols

A_{gs}	area of the s-g interface contained in the averaging volume, V, m^2
A_s	specific surface area, m^{-1}
$\mathbf{b_{ii}}$	vector field that maps $\nabla \langle T_i \rangle^i$ onto $\tilde{T}_i$ in LTNE model
Bi	Biot number
$c_1 - c_3$	coefficients associated with thermal conductivity
$c_{p,i}$	heat capacity of the i-phase, $\mathrm{J\,kg^{-1}\,K^{-1}}$
d_{par}	particle diameter, m
D_t	tube diameter, m
f	coefficients associated with Nusselt number
$\mathbf{F}$	Forchheimer correction tensor
Gr	Grashof number
H	tube length, m
h_s	interstitial heat transfer coefficient, $\mathrm{W\,m^{-2}\,K^{-1}}$
h_v	volumetric heat transfer coefficient, $\mathrm{W\,m^{-3}\,K^{-1}}$
$\mathbf{I}$	Identity tensor
k_i	thermal conductivity of the i-phase, $\mathrm{W\,m^{-1}\,K^{-1}}$
$\mathbf{k_{i,eff}}$	effective thermal conductivity tensor of the i-phase, $\mathrm{W\,m^{-1}\,K^{-1}}$
$\mathbf{K}$	permeability tensor, m^2
K	permeability scalar, m^2
K_{eff}	effective permeability scalar, m^2
L	the length of the fluid region, m
M	gas molar mass, $\mathrm{kg\,mol^{-1}}$
$\mathbf{n_{gs}}$	outwardly directed unit normal vector pointing from the gas phase toward the solid phase, $\mathbf{n_{gs}} = -\mathbf{n_{sg}}$
Nu	Nusselt number based on h_v
p	gas pressure, $\mathrm{kg\,m^{-1}\,s^{-2}}$

$\langle p \rangle^g$	Intrinsic average pressure, $\mathrm{kg\,m^{-1}\,s^{-2}}$
Pe	Peclet number
Pr	Prandtl number
R	ideal gas constant, $\mathrm{J\,K^{-1}\,mol^{-1}}$
Re	Reynolds number based on the pore diameter
Ri	Richardson number
T_i	point temperature in the i-phase, K
$\langle T_i \rangle^i$	initrinsic phase average temperature in the i-phase, K
$\tilde{T}_i$	the spatial deviation temperature in the i-phase, $\tilde{T}_i = T_i - \langle T_i \rangle^i$, K
$\overline{T_i}$	average temperatures obtained from the micro-scale simulations, K
$\mathbf{u}$	Darcy velocity, $\varepsilon_g \langle \mathbf{v_g} \rangle^g$, $\mathrm{m\,s^{-1}}$
$\mathbf{v_g}$	velocity of the gas phase, $\mathrm{m\,s^{-1}}$
$\langle \mathbf{v_g} \rangle^g$	intrinsic phase average velocity of the gas, $\mathrm{m\,s^{-1}}$
$\langle \mathbf{v_g} \rangle$	superficial average velocity, $\mathrm{m\,s^{-1}}$
$\tilde{\mathbf{v}}_{\mathbf{g}}$	the deviation of gas velocity, $\tilde{\mathbf{v}}_{\mathbf{g}} = \mathbf{v_g} - \langle \mathbf{v_g} \rangle^{\mathbf{g}}$, $\mathrm{m\,s^{-1}}$
V	averaging volume, m^3
$\mathbf{X}$	Forchheimer tensor, m^{-1}

Special symbols

$\langle \rangle$	phase average
$\langle \rangle^i$	intrinsic average

Subscripts

$\perp$	transverse
con	conductivity
dis	dispersion
g	gas
s	solid
tor	tortuosity

such as rocks, sand, and gravel are used in sensible heat storage systems, where they are arranged in a packed bed structure inside a container. To optimize the design of TES systems, the coupled heat and momentum transfer between the carrier fluid and the packed-bed material needs to be well understood and modeled. Fluid flow processes in a packed bed can be modeled by using either a micro- or macro-scale approach. Micro-scale models consider pore-scale behavior, including pore heterogeneity and fluid–solid interactions [8–10]. In contrast, macro-scale models generally treat the packed bed as a homogeneous and isotropic medium, where transfer phenomena are described by averaged equations [11–15].

In order to bridge micro- and macro-scale models of packed beds, upscaling methods such as the homogenization theory and the volume-averaging technique establish the relationships between variables at different scales. In an equivalent porous continuum model at macro-scale, the value at each point of a macroscopic variable is the volume average value of the corresponding microscopic variable in a representative elementary volume (REV). In macroscopic models, some phenomenological parameters are introduced to characterize the relationships between macroscopic variables. For instance, permeability K, and the Forchheimer coefficient β describe the linear and nonlinear interrelations between pressure drop and velocity for low- and high-velocity flows respectively [16,17]; effective thermal conductivity k_{eff} and interfacial heat transfer coefficient h_s characterize the heat transfer process within a packed bed [13]. Several correlations have been developed from experiments such as the Ergun or Kozeny–Carman expressions for pressure drop [18,19], and Whitaker or Wakao expressions [20,21] for heat transfer characteristics. Furthermore, by means of numerical methods at the micro-scale, correlations for k_{eff} or h_s have been obtained [18,22–25]. However, under some specific conditions, like high temperature and high Reynolds flows, these correlations need to be enhanced to accommodate the substantial changes in gas properties and flow behavior. Otherwise, there is a possibility that the

model may not accurately capture the micro-scale heterogeneity of the porous structure, potentially affecting the reliability of the numerical results. To investigate the pressure drop and heat transfer characteristics of a randomly packed bed at high temperatures, our work employs both micro- and macro-scale approaches and compares the respective features of temperature obtained from these different scales.

To solve a micro-scale problem, the first step is to build a microstructure. Regular structures such as arrays of square and staggered arrangements of square cylinders have been employed [26,27]. With the progress of the resolution of computed micro-tomography and computer resources, one can obtain a more realistic microstructure of the packed bed directly by using X-ray computed tomography (XCT) scanning [8,28] or alternatively, generate the packed bed structure by using the discrete element method (DEM) after providing the geometry of a single particle with its diameter d_{par} [18,23,29]. According to the obtained microstructure, the global packed bed region consists of the solid and the fluid regions. The velocity and pressure variables only need to be solved within the fluid region using the Navier–Stokes equations. Specifically, for low Reynolds numbers and constant temperature conditions, the fluid is treated as incompressible [18,25,30]. However, for high Reynolds number, incidentally, high Mach number, or when temperatures vary, the fluid is considered compressible. For the temperature distribution in the packed bed, due to the thermal resistance between particles and gas within the packed bed, a temperature jump occurs across the solid–fluid interface. Therefore, the temperatures of the solid and fluid regions need to be solved separately [25]. To characterize the relative significance of convective heat transfer at the interface compared to conductive heat transfer within the solid, we introduce a dimensionless number, Biot number ($Bi = h_s d_{par}/k_s$). For very small Biot numbers ($Bi \ll 0.1$), heat transfer within the solid can be considered instantaneous. As a result, it is sufficient to solve the heat transfer equation within the fluid region, and the heat transfer within the solid can be neglected. It is valid in a steady state. In a transient state, the solid thermal inertia would have to be accounted for.

After obtaining microscopic numerical results, the closure method and the integral method enable to determine various physical quantities corresponding to different macroscopic models. The principle of these two methods is to integrate microscopic-scale variables on solid–fluid interfaces or within the region to obtain macroscopic quantities. The closure method is applicable to periodic unit cells or sufficiently large volume domains that account for all characteristics of the pore structure. The integration method can be applied to diverse geometries. The heat transfer in a packed bed at the macro-scale can be studied using either the local thermal equilibrium (LTE) or local thermal non-equilibrium (LTNE) model [11,31,32]. The LTE model assumes that the fluid and solid rapidly reach an equilibrium state thus it only involves one global temperature equation, where the effective conductivity $\mathbf{k_{eff}}$ needs to be determined. The LTNE equation suits the condition where the thermal conductivity of solid and fluid phases exhibit a large difference or heat transfer involves internal heat generation [33,34]. Therefore it leads to a two-temperature model involving three quantities: gas and solid effective thermal conductivities $\mathbf{k_{g,eff}}$ $\mathbf{k_{s,eff}}$ respectively, and volumetric heat transfer coefficient h_v. In many works, $\mathbf{k_{g,eff}}$ and $\mathbf{k_{s,eff}}$ were straightforwardly calculated as the product of the corresponding porosity and thermal conductivity of the respective phase, as following expressions: $\mathbf{k_{g,eff}} = \varepsilon_g k_g \mathbf{I}, \mathbf{k_{s,eff}} = \varepsilon_s k_s \mathbf{I}$. Wakao et al. [21] considered the effect of fluid dispersion in the longitudinal ($\parallel$) and transverse ($\perp$) flow directions and modified the expression of $\mathbf{k_{g,eff}}$ by introducing the product of the Reynolds number and the Prandtl number with a coefficient. Quintard et al. [11] provided a theoretical formulation, stating that $\mathbf{k_{g,eff}}$ is influenced by three factors: thermal conduction, tortuosity, and dispersion, resulting in its anisotropic behavior [7,11,35]. For the volumetric heat transfer coefficient h_v, it can be determined through the integration method, which reads as follows: [36],

$$h_v = \frac{\frac{1}{V} \int_{A_{gs}} k_g \nabla T_g \cdot \mathbf{n}_{gs} dA}{\langle T_s \rangle^s - \langle T_g \rangle^g} \tag{1}$$

where V is volume of the global region and A_{gs} is the solid–fluid surface. T_i and $\langle T_i \rangle^i$ denote the point temperature in the i-phase and the intrinsic phase average temperature for the i-phase, $\langle T_i \rangle^i = \frac{1}{V_i} \int_{V_i} T_i dV$, V_i is the volume of the i-phase contained within the volume V. $\mathbf{n}_{gs}$ is the outward unit normal vector, which points from the gas phase towards the solid phase.

The objective of our work is to apply a multi-scale approach to investigate the pressure drop and heat transfer coefficients in a randomly packed bed at high temperatures. Fig. 1 schematically shows the present multi-scale modeling strategy, where streamlines are colored based on the velocity or temperature. To start, we build a 3D randomly packed bed filled with spherical particles via the DEM software LIGGGHTS. Two microscopic models are solved in this packed bed for different situations: the first one is an incompressible flow under constant temperature, characterized by the incompressible Navier–Stokes equations, the solutions are then used to obtain permeability and the Forchheimer coefficient. The second is a transient compressible flow, with high-temperature gas (800 K) entering from the inlet, by a model coupling mass and momentum conservation equations for the fluid phase, and energy equations for fluid and solid phases, respectively. Once the temperature field is obtained, h_v can be evaluated by Eq. (1). Next, in the macroscopic simulation, a 2D axisymmetric structure is designed to mimic the three-dimensional cylindrical structure. The macroscopic governing equations consist of the macroscopic mass and momentum equations and the LTNE model. The effective thermal conductivities and heat transfer coefficients were optimized by using an inverse analysis approach, wherein the governing equations are solved at each iteration to approximate the volume average of the microscopic temperature. The article is organized as follows. In Section 2, we generate the packed bed structure and present the numerical methods for two microscopic models. In Section 3, we present the results of micro-scale simulations and investigate the pressure drop at room temperature and the heat transfer coefficient at high temperatures. In Section 4, the numerical method and results at the macro-scale are presented. It is based on a multi-objective optimization method to minimize errors between the data obtained from the two scales. Some concluding remarks are given in Section 5.

2. Numerical methods at the micro-scale

In this section, we first solve the classical Navier–Stokes equations, assuming constant thermophysical properties, to obtain the pressure drop. This information is then utilized to determine permeability and Forchheimer coefficients. Furthermore, we solve coupled heat and momentum transfer equations, considering variable thermophysical properties, to simulate the transient temperature distribution of gas and solid during the heat transfer process. This enables us to determine the heat transfer coefficient. The first subsection outlines the generation of packed beds using the discrete element method (DEM). Subsequently, we introduce the mathematical model and boundary conditions required for solving the flow and heat transfer equations.

2.1. Random packed bed generation

To generate a geometric representation of randomly packed beds that accurately reflects the stacking structure, we employed the open-source software LIGGGHTS [37]. This software utilizes the discrete element method (DEM) to simulate the effects of gravity and friction forces on particles within the packed bed, creating a realistic medium using advanced mathematical functions [38]. Spherical particles are inserted at the top of the tube and descend to the flat surface at the bottom under the influence of gravity. The software individually tracks each particle's trajectory and collisions, applying Newton's laws of translational and rotational momentum, which account for the possibility of an inelastic rebound. The packing process ceases when the
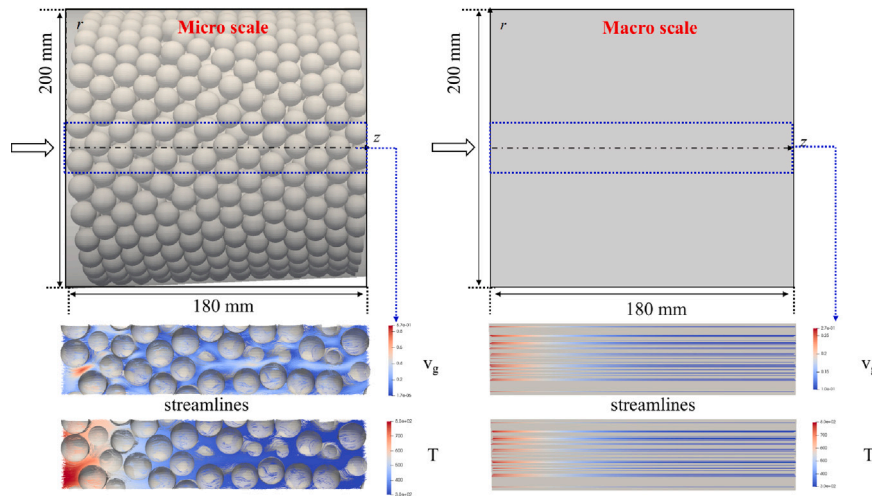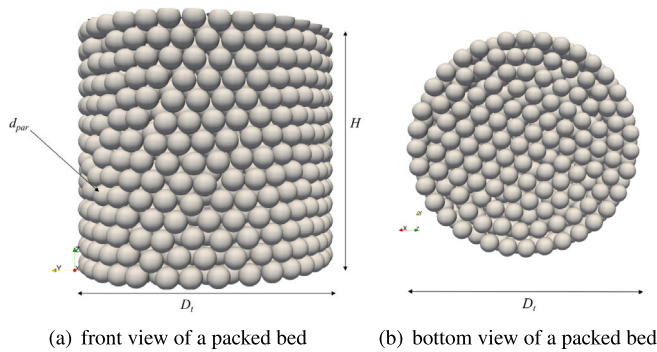
Fig. 1. Multi-scale modeling strategy.

(a) front view of a packed bed   (b) bottom view of a packed bed

Fig. 2. Views of the front and the bottom of packed beds with spherical particles.

Table 1
Simulation parameters for generating the packed bed.

Parameter	Value
particle diameter, d_{par} (mm)	16
diameter aspect ratio, D_t/d_{par}	12.5
number of particles, N	1638
insertion height, H (mm)	180
density of glass beads particles (kg/m³)	2500
Young's modulus, particle and wall (Pa)	7.3×10^{10}
Poisson's ratio, particle and wall	0.228
coefficient of restitution, particle and wall	0.9
coefficient of friction, particle–particle	0.05

kinetic energy of the particles dissipates, and the particles come to rest. Simulation parameters are listed in Table 1.

Fig. 2 presents a 3D view of the randomly packed beds filled with spherical particles. The tube has a diameter of 200 mm and a height of 180 mm, while the spherical particles have a uniform diameter of 16 mm. The generation process requires about 10 h of computational time on a single thread (Intel Core CPU i9-13900K @ 3.00 GHz, RAM 32 Go 4400 MHz).

To validate the accuracy of the generated packed bed model, we calculated the global porosity ε_g and compared it with the classical correlation proposed by Muller [39,40], which is defined and expressed as follows:

$$\varepsilon_g = 1 - \frac{V_{solid}}{V_{total}} = 0.365 + 0.22/(D_t/d_{par}), \qquad \text{for } D_t/d_{par} \geq 2.02 \qquad (2)$$

where V_{solid} and V_{total} represent the volume of spherical particles and the total volume of the packed bed, respectively. This correlation can be

used for fixed packed beds of uniformly sized spheres with $D_t/d_{par} \geq 2.02$ [40]. The volume of spherical particles was determined using a ParaView filter (Integrate Variables [41]). The global porosity of the randomly packed bed of spheres was found to be 0.379, while the value calculated from Eq. (2) was 0.382, resulting in a relative error of 0.7%. Considering the fact that the wall will induce a packing different from the center, a zone that might be prone to channeling. These results further confirm the reliability and accuracy of the DEM method used in this study for generating randomly packed beds of spheres.

2.2. Numerical model

The numerical model shown in Fig. 3 consists of a three-dimensional geometry with different regions defined as follows: fluid domains (flow1 and flow2) and a porous domain (packed bed).

In the first case, the pressure drop was calculated to determine the permeability and the Forchheimer coefficient by solving the classical Navier–Stokes equations. The fluid was assumed to be incompressible in both the fluid and porous domains, and the thermophysical properties of the fluid were assumed to be constant. The permeability and the Forchheimer coefficient were then obtained by setting different inlet velocities.

In the second case, the coupled heat and momentum transfer equations were solved in transient regime to calculate the heat transfer coefficient. High-temperature air with $T_g = 800$ K was used to heat low-temperature particles with $T_s = 300$ K. The summary of the assumptions underlying the model are as follows: (1) The fluid flow was considered incompressible and laminar. (2) The temperature-dependent relationships for the thermophysical properties of the gas and solid phases were taken into account. (3) The inter-particle and intra-particle radiation heat transfer were neglected, which is a reasonable assumption for temperatures not exceeding 800 K [42]. (4) The effect of gravity on gas flow was ignored, which is a valid assumption for cases with Richardson numbers much less than one, as explained in Appendix A. (5) The wall effect on the heat transfer rate was neglected due to the ratio of reactor diameter to particle diameter (D_t/d_{par}) being greater than 10 [43]. Additional details will be discussed below.

2.2.1. Mathematical model and numerical implementation

For the first case, only the mass and momentum equations were solved. The flow in both the fluid domains (flow1 and flow2) and the porous domain (packed beds) was considered to be transient,
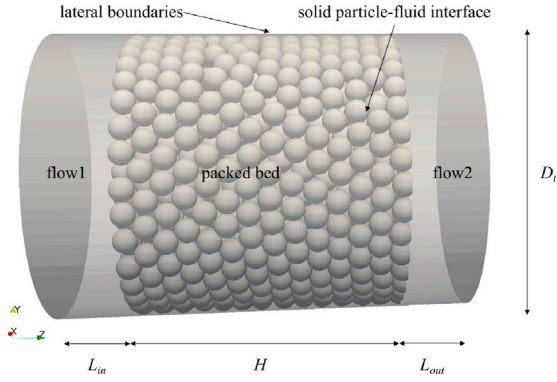
Fig. 3. Three-dimensional numerical model of the packed bed.

incompressible, and without heat transfer. The mass and momentum equations are given by Eq. (3) [44]:

$$\begin{cases} \nabla \cdot \mathbf{v_g} = 0 \\ \rho_g \left(\dfrac{\partial \mathbf{v_g}}{\partial t} + \mathbf{v_g} \cdot \nabla \mathbf{v_g} \right) = -\nabla p + \mu_g \nabla^2 \mathbf{v_g} \end{cases} \quad (3)$$

where $\mathbf{v_g}$ and p represent the velocity and pressure of the fluid, respectively. ρ_g and μ_g denote the density and dynamic viscosity of the fluid.

For the second case, the transient compressible laminar Navier–Stokes equations and energy equations are used to model the flow domains (flow1 and flow2). In the porous domain (packed beds), heat transfer is modeled using conduction in both phases and convection in the fluid phase. The coupling between the different regions is achieved by ensuring the conservation of mass and continuity of temperatures and heat fluxes at the interfaces. The governing equations for compressible gas flow at the micro-scale are given [44]:

$$\begin{cases} \partial_t \rho_g + \nabla \cdot (\rho_g \mathbf{v_g}) = 0 \\ \rho_g \left(\dfrac{\partial \mathbf{v_g}}{\partial t} + \mathbf{v_g} \cdot \nabla \mathbf{v_g} \right) = -\nabla p + \mu_g \nabla^2 \mathbf{v_g} \\ \rho_g c_{p,g} \dfrac{\partial T_g}{\partial t} + \rho_g c_{p,g} \mathbf{v_g} \cdot \nabla T_g = k_g \nabla^2 T_g \\ \rho_s c_{p,s} \dfrac{\partial T_s}{\partial t} = k_s \nabla^2 T_s \end{cases} \quad (4)$$

where T_g and T_s are respectively the temperatures of the fluid and the solid. $c_{p,i}$ and k_i denote the specific heat at constant pressure and thermal conductivity of the i phase.

Table 2 presents the boundary conditions used for the first case, which involves only the fluid domain and includes only pressure and velocity terms. The *fixed value* condition is used to specify a constant value for the inlet velocity. At the solid particle–fluid interface the *no slip* condition is applied to the packed bed domain. At the lateral boundaries, two different kinds of boundary conditions can be applied: *no slip* or *symmetry*, the latter assuming that the domain is a subset of an infinite periodic domain [18]. So we use *no slip* boundary conditions for the lateral boundaries. The pressure boundary condition is set as *zero gradient* to ensure that the pressure gradient perpendicular to the wall is zero. The thermophysical properties of air were evaluated at room temperature (293 K), where the density of air is 1.20 kg/m³, dynamic viscosity is 1.90×10^{-5} Pa s, and the gas molar constant is 28.96 g/mol. The numerical model was implemented using the Porous material Analysis Toolbox based on OpenFoam (PATO) [45]. The classical Navier–Stokes equations (Eq. (3)) were solved with the *pimpleFoam* solver, which is a combination of the pressure-implicit split-operator (PISO) and the semi-implicit method for pressure-linked equations (SIMPLE) algorithms [46]. Second-order schemes, with flux limiters, were used for spatial discretization.

Table 3 presents the initial and boundary conditions for the transient heat transfer problem, which includes both the fluid and porous domains. The inlet velocity and outlet pressure for the fluid phase are set to fixed values. The *no slip* boundary condition is applied at the sides and interface to set the velocity to zero. The *fixedFluxPressure* condition is imposed at the inlet to enforce a specific pressure gradient, ensuring that the boundary flux is determined by the specified velocity boundary condition.

The thermo-physical properties of both gas (air) and the solid (glass) vary with temperature and are detailed following the work of Wang et al. [47]. The density of air, ρ_g, is calculated using the perfect gas law, while the values for the heat capacity, $c_{p,g}$, dynamic viscosity, μ_g, and thermal conductivity, k_g, are obtained from the NASA-9 database [48,49]. The density of glass, ρ_s, is assumed to be constant at 2500 kg/m³. The thermal conductivity, k_s, and the heat capacity, $c_{p,s}$ can be found as follows [48]:

$$\begin{cases} k_s = 0.59206 + 0.00062T_s + 1.0013 \times 10^{-6}T_s^2 - 2.778 \times 10^{-10}T_s^3 \\ c_{p,s} = 316.506 + 2.0745T_s - 0.00199T_s^2 + 7.4369 \times 10^{-7}T_s^3 \end{cases} \quad (5)$$

The thermophysical properties of both phases are summarized in Table 4.

A multi-block approach is used, where different sets of equations are solved at each time step with appropriate boundary conditions, computed from the mass and energy balances at the interfaces. The equations in the porous and fluid domains are computed using the conjugate heat transfer solver (chtMultiRegionFoam) of OpenFOAM v9. Fluid flow is solved using *pimpleFoam* solver. The equations are solved in series, with appropriate mesh refinement and time steps to ensure that the order of convergence is reached, as described in Section 2.2.2.

2.2.2. Mesh and time step convergence analysis

In the first case, only the mass and momentum equations need to be solved for the fluid phase in both fluid and porous domains, and thus only the fluid phase required meshing. In contrast, in the second case, the energy equations for both phases need to be solved separately, which requires meshing for both phases. We chose to mesh the fluid domain and porous domain using the automatic meshing program called *snappyHexMesh* within the OpenFOAM CFD framework (v2206 version) [50]. This tool is a mesh manipulation software that allows users to refine a given background mesh to their desired configuration. The meshing algorithm works through three primary steps (Fig. 4). First, a background mesh is generated, followed by the overlaying of particle surfaces onto the mesh (Fig. 4(a)). The algorithm identifies cells intersected by the particle surfaces and subdivides them into eight parts, creating mesh refinement near the body surface (Fig. 4(b)). Subsequently, mesh points near the body surface are moved to align with the surface, ensuring that the boundary surfaces of the mesh conform closely to the prescribed geometry (Fig. 4(c)). In this step, the background mesh is removed, and the mesh is retained within the fluid and solid regions. The final step involves further refining the mesh within the fluid domain, especially at the fluid–solid interface and within the solid itself. The quality of the final mesh (Fig. 4(d)) depends highly on various parameter settings. Once the parameter configuration process is established, the next step is to perform a mesh independence verification to ensure that the final mesh does not influence the simulation results. Here, a simplified meshing technique illustration has been provided using only four contacted particles. For packed beds containing thousands of particles, the meshing process becomes more complex, but the meshing algorithm remains similar. It is worth noting that, due to the stacking of particles, the contact angles between some of them can become quite small. In such cases, it is essential to utilize the "gapLevel" (value 1) keyword to enable automatic refinement in small gaps and the "minCellFraction" (value 0.001) keyword to delete small regions. This ensures the correct generation of the mesh and limits bridging between the particles. To face the need

Table 2
Boundary conditions for gas flow simulation.

Fluid	Inlet	Outlet	Solid particle–fluid interface	Lateral boundaries
$\mathbf{v_g}$	Fixed value	Zero gradient	No slip	No slip
p	Zero gradient	Fixed value	Zero gradient	Zero gradient

Table 3
Boundary conditions for coupled heat simulation.

Region	Initial conditions	Boundary conditions			
Fluid		Inlet	Outlet	Solid particle-fluid interface	Lateral boundaries
$\mathbf{v_g}$	0 m/s	Fixed value	pressureInletOutletVelocity	No slip	No slip
p	0 Pa	fixedFluxPressure	Fixed value	Zero gradient	Zero gradient
T_g	300 K	Fixed value (800 K)	Zero gradient	$k_g \nabla T_g = k_s \nabla T_s$	Zero gradient
Solid				Interface	Solid
T_s	300 K			$k_s \nabla T_s = k_g \nabla T_g$	Zero gradient

Table 4
Properties of gas (air) and solid (glass) as a function of temperature.

T (K)	Gas			Solid	
	$c_{p,g}$ (J kg^{-1} K^{-1})	μ_g (kg m^{-1} s^{-1})	k_g (W m^{-1} K^{-1})	$c_{p,s}$ (J kg^{-1} K^{-1})	k_s (W m^{-1} K^{-1})
290	1010.4	1.909×10^{-5}	0.0278	768.75	0.850
340	1013.1	2.105×10^{-5}	0.0309	820.82	0.909
390	1017.5	2.306×10^{-5}	0.0340	866.73	0.971
440	1023.9	2.507×10^{-5}	0.0372	907.02	1.035
490	1032.1	2.710×10^{-5}	0.0405	942.27	1.105
540	1041.5	2.914×10^{-5}	0.0441	973.03	1.177
590	1055.7	3.120×10^{-5}	0.0476	1000.48	1.249
640	1067.6	3.299×10^{-5}	0.0508	1024.03	1.326
690	1079.8	3.471×10^{-5}	0.0541	1044.78	1.405
740	1092.1	3.643×10^{-5}	0.0574	1063.27	1.486
800	1104.1	3.815×10^{-5}	0.0607	1080.07	1.569

(a) Background mesh and fluid and solid regions

(b) First refinement of the background mesh

(c) Snapping of the refined mesh to the body surface
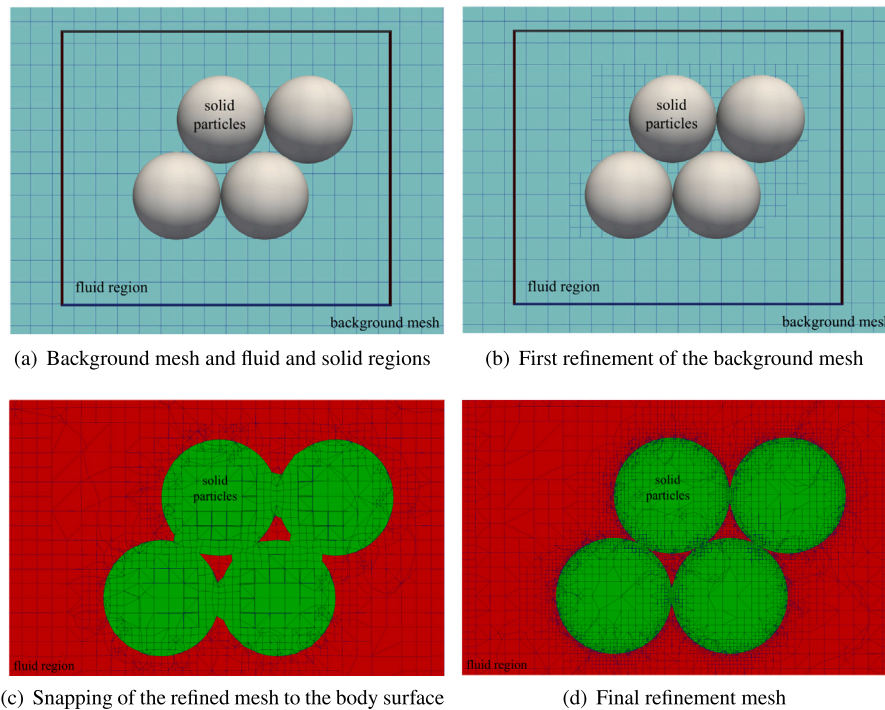
(d) Final refinement mesh

Fig. 4. Meshing technique diagram.

for computational power, we used part the MCIA cluster - 4 nodes, 32 cores (Intel Xeon Gold SKL-6130 @2,1 GHz) and 92 Go per node.

Mesh and time step convergence for this model is found by systematically decreasing values for each of the mesh sizes and time steps until the solution (average local gas temperatures) minimally changes and

can be performed independently of each other. A mesh and time step convergence study was conducted with pressure residuals remained below 10^{-6} and velocity residuals below 10^{-8} at the highest inlet velocity ($|\langle v_g \rangle| = 0.5$ m/s, $Re = \rho_g |\langle v_g \rangle| d_{par}/\mu_g = 505.3$) due to the presence of the sharpest gradients. The results of the mesh and time
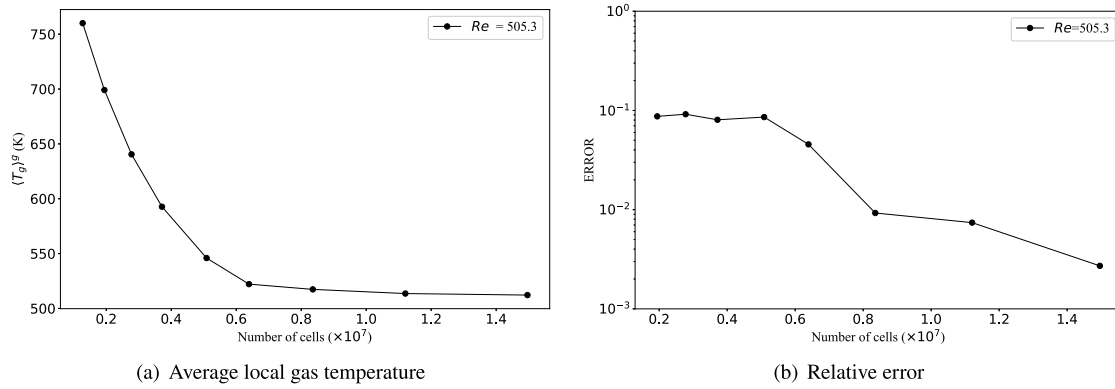
(a) Average local gas temperature

(b) Relative error

Fig. 5. Mesh convergence test.

(a) Average local gas temperature
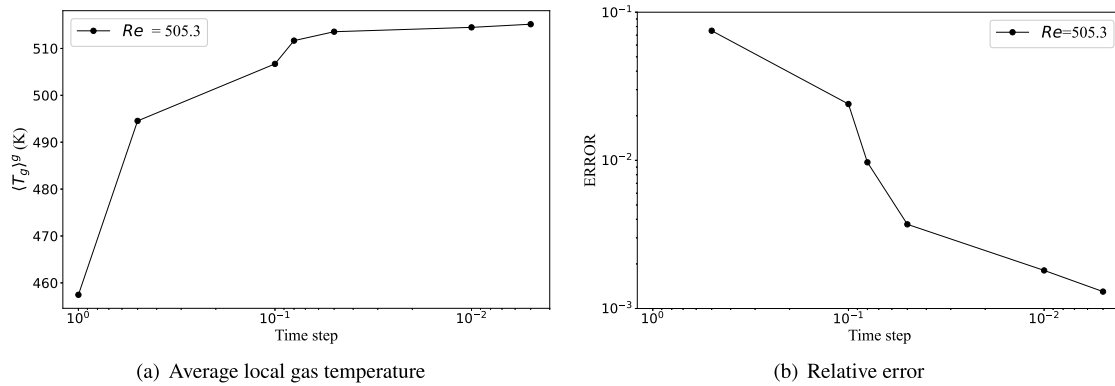

(b) Relative error

Fig. 6. Time step convergence test.

step convergence analysis at $t = 400$ s are presented in Figs. 5 and 6, respectively. In performing mesh convergence testing, the time step is kept constant at 10^{-3} s. The average local gas temperatures are calculated as the number of cells increases as shown in Fig. 5(a). The behavior of the numerical error is shown in Fig. 5(b). The error is defined as follows,

$$\text{error} = \frac{|\langle T_g \rangle_{n+1}^g - \langle T_g \rangle_n^g|}{\langle T_g \rangle_{n+1}^g} \qquad (6)$$

where the index n denotes the simulation with mesh before refinement. The results suggest that when the number of cells surpasses 11.2 million, the error gradually decreases until it reaches around 7.4×10^{-3}. Therefore, 11.2 million cells are acceptable for the numerical simulations. Constant time steps with a user-set value are used in the simulations. When the time step decreases from 5×10^{-2} s to 1×10^{-2} s as shown in Fig. 6(b), there is no noticeable evolution in the value of averaged local gas temperature $\langle T_g \rangle^g$ as shown in Fig. 6(a). Therefore, the time step is set to 5×10^{-2} s. Fig. 7 provides detailed views of the meshed geometry. In Fig. 7(a) and (b), the red regions represent individual particles, while the blue regions represent the fluid. Fig. 7(c) is an enlarged view of a portion of the particles in a, showing the refined meshing at the interface between the particles and the fluid. Moreover, to ensure the accuracy of the present numerical model, it was compared with the experimental study reported by Wakao et al. [51], as detailed in Appendix B.

3. Simulation results at the micro-scale

In this section, we presented the results of two micro-scale simulation cases. In the first case, the inlet velocity of the gas was varied from 1×10^{-5} to 0.5 m/s, resulting in an increase in the Reynolds number from 0.01 to 505.3, and the pressure drop was calculated. Given that

the laminar flow limit inside a packed bed typically falls between 500 to 600 [52], this range of inlet velocities is reasonable. In the second case, the same velocity variation was applied, and the temperature distribution inside the packed bed was obtained by solving the governing equations, and the heat transfer coefficient was subsequently calculated.

3.1. Pressure drop

To upscale the pore-scale problem in porous media, the homogenization theory [53] or the volume-averaging technique [54] was proposed. The macroscopic model given by Eq. (7) was demonstrated[54],

$$\begin{cases} \nabla \cdot \langle \mathbf{v_g} \rangle = 0 \\ \langle \mathbf{v_g} \rangle = -\frac{1}{\mu_g} \mathbf{K} \cdot \nabla \langle p \rangle^g - \mathbf{F} \cdot \langle \mathbf{v_g} \rangle \end{cases} \qquad (7)$$

where $\langle \mathbf{v_g} \rangle$ is the superficial average velocity, referred to as the filtration velocity or Darcy velocity, and $\langle p \rangle^g$ is the intrinsic average of the pressure [55]. $\mathbf{F}$ is the Forchheimer correction tensor ($\mathbf{K} \cdot \beta |\langle \mathbf{v_g} \rangle| \rho_g / \mu_g$), where $\mathbf{K}$ is the permeability tensor, β is the Forchheimer coefficient tensor. $\langle \varphi_i \rangle$ and $\langle \varphi_i \rangle^i$ are the superficial and intrinsic phase averages of any quantity φ_i associated with the i-phase, respectively. In this case, we assumed packed beds to be isotropic porous materials. When the flow velocity is small, the second term $\mathbf{F} \cdot \langle \mathbf{v_g} \rangle$ in Eq. (7) can be neglected, and Darcy's law is validated. The numerical results for varying Reynolds numbers ($Re = \rho_g |\langle \mathbf{v_g} \rangle| d_{par} / \mu_g$) are illustrated in Fig. 8. Fig. 8(a) and (b) display the variations of pressure gradient and effective permeability as a function of Reynolds number, respectively. The effective permeability in one-dimensional flow is calculated using Eq. (8).

$$K_{eff} = -\langle v_g \rangle \cdot \mu_g \cdot \frac{H}{\Delta \langle p \rangle^g} = -\frac{\mu_g^2}{\rho_g d_{par}} \frac{H}{\Delta \langle p \rangle^g} Re \qquad (8)$$
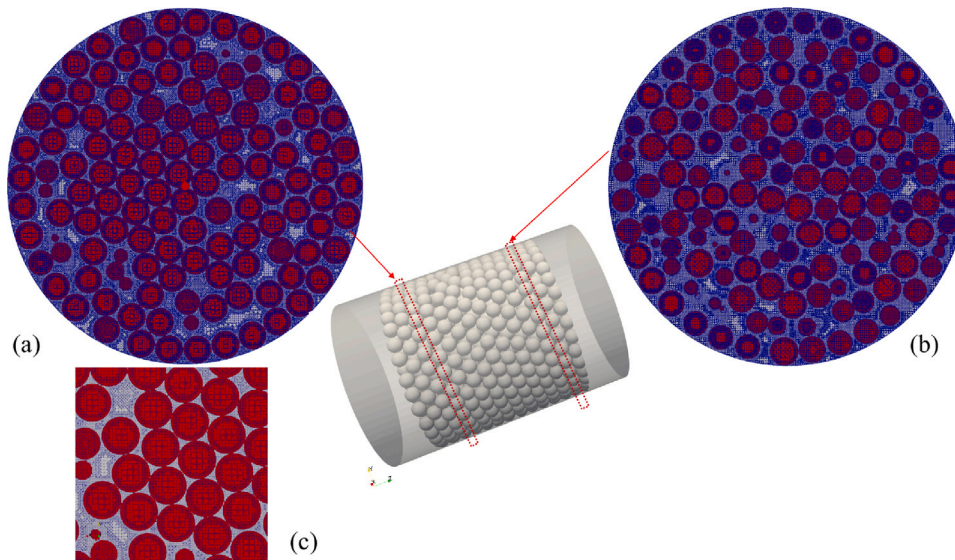
Fig. 7. Some details of the meshed geometry. (a), (b) Mesh on the two cross-sections. (c) An enlarged view of a portion of the particles.
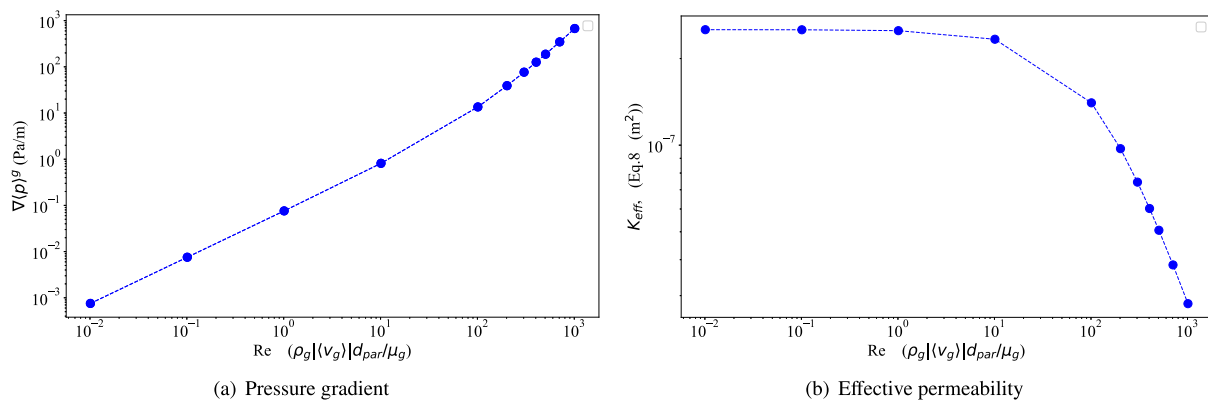

(a) Pressure gradient

(b) Effective permeability

Fig. 8. Computed pressure gradient and effective permeability with increasing Reynolds number.

Table 5
Permeability K and Forchheimer coefficient β in packed beds filled with spheres.

Permeability, K (m^2)	Forchheimer coefficient, β (m^{-1})
2.451×10^{-7}	1.188×10^3

In this case, the pressure gradient exhibits a non-linear relationship, and the flow region covers both Darcy and Forchheimer flow regimes, as demonstrated in Fig. 8(a). This observation is further supported by Fig. 8(b), where the constant K_{eff} corresponds to the Darcy flow regime. For Re less than 10.1, the pressure gradient increases linearly, and the effective permeability K_{eff} remains constant, indicating a Darcy flow regime. For Re higher than 10.1, the pressure gradient increases nonlinearly, accounting for inertial effects. To compute the Forchheimer coefficient β, a rearranged form of the Forchheimer equation for one-dimensional flow is presented in Eq. (9).

$$-\frac{\Delta\langle p\rangle^g}{H} \cdot \frac{1}{\langle v_g\rangle} \cdot \frac{1}{\mu_g} = \beta(\rho_g|\langle v_g\rangle|\frac{1}{\mu_g}) + \frac{1}{K} \tag{9}$$

We introduced two new variables, X and Y, $X = \rho_g|\langle v_g\rangle|\frac{1}{\mu_g}$, $Y = -\frac{\Delta\langle p\rangle^g}{H} \cdot \frac{1}{\langle v_g\rangle} \cdot \frac{1}{\mu_g}$, thus given by $Y = \beta X + \frac{1}{K}$, to compute the values of β using the least-squares approximation method, as displayed in Fig. 9. The values for both K and β are presented in Table 5.

To validate our simulation results, we have chosen to compare them with the results calculated using the Ergun equation (Eq. (10)) [56], in which these two parameters are treated as scalars.

$$K = \frac{d_{par}^2 \varepsilon_g^3}{150\varepsilon_s^2}, \qquad \beta = \frac{1.75\varepsilon_s}{d_{par}\varepsilon_g^3} \tag{10}$$

where the gas volume fraction (porosity, ε_g) is calculated using the Muller correlation (Eq. (2)) [40]. The values of K and β calculated using Eq. (10) are 2.51×10^{-7} m^2 and 1.206×10^3 m^{-1}, respectively, with a respective error of 2.44% and 1.52% compared to the simulated values. This indicates that the model used in this work can be used to simulate laminar flow in both the Darcy and the Forchheimer flow regimes.

3.2. Volumetric heat transfer coefficient

In this subsection, we start by examining the temperature and velocity distribution within the packed bed at a specific inlet velocity. The impact of the inlet velocity and solid thermal conductivity on the volumetric heat transfer coefficient is then summarized.

3.2.1. Temperature and velocity distributions

As a large number of simulations were carried out, a representative case with an inlet gas velocity of 0.1 m/s ($Re = 101$ at room temperature) was selected to describe the temperature distribution of gas and
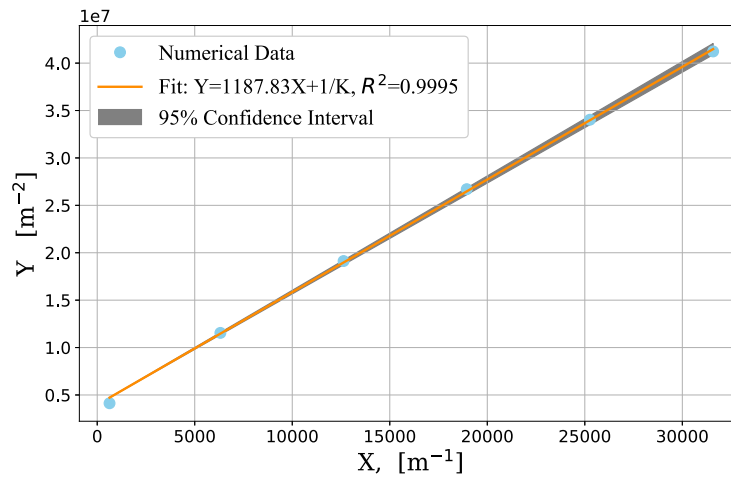
Fig. 9. Relationship between terms X ($\rho_g|\langle v_g \rangle|/\mu_g$) and Y ($\Delta\langle p \rangle^g/(H\langle v_g \rangle \mu_g)$).
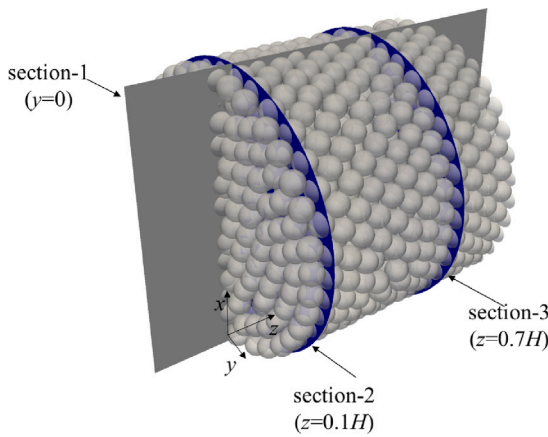

Fig. 10. Selected sections in a randomly packed bed of spheres.

particles within the packed bed, where the inlet gas temperature was 800 K and the initial temperature of the spherical particles was 300 K, and the internal heat transfer in the spherical particles was considered. To illustrate the velocity and temperature distribution inside the packed beds, we selected three typical cross-sections, as shown in Fig. 10, where Section 1 is located at $y = 0$, Section 2 is located at $z = 0.1H$, and Section 3 is located at $z = 0.7H$. The packed bed can be further divided into two parts: the spherical solid particles and the fluid region between the particles.

The temperature distribution in Section 1 of the randomly packed bed with uniform spheres is presented in Fig. 11, which was selected at $t = 1000$ s to display the temperature distribution due to the transient heat transfer of air. Fig. 11(a) shows the overall temperature field of both gas and solid in the plane, while Fig. 11(b) and (c) respectively show the temperature fields of the gas and solid. As shown in Fig. 11, the temperature distribution in the packed bed is non-uniform. Hot gas enters from the left side of the domain and cools down as it flows towards the right through the sphere domain. The gas temperature on the left side of the bed reaches up to 790 K, while the gas on the right side remains at room temperature. Similarly, for the solid phase, the solid near the inlet is heated to around 650 K, while the solid at the outlet remains at room temperature. To analyze the temperature distribution at the interface between gas and solid and the temperature distribution inside the solid, we selected appropriate positions in Fig. 11(a) and (c), magnified the temperature distribution and plotted temperature contour maps. The results are shown in (d)

and (e). In Fig. 11(d), the temperature contour intervals are 20 K and it can be seen that the temperature difference between the gas and solid at their interface reaches 30 K, proving that the local gas and solid temperatures in the packed bed are not in equilibrium. In Fig. 11(e), the temperature of the solid is unevenly distributed within the same sphere with a maximum temperature difference of 30 K, indicating that the internal heat conduction of the solid must be considered in this case.

Fig. 12 provides a complementary analysis to the temperature distribution presented in the previous paragraph. It shows the distribution of gas velocity (v_g), Reynolds number ($Re = \rho_g v_g d_{par}/\mu_g$), and Prandtl number ($Pr = \mu_g c_{p,g}/k_g$) in Section 1 of the packed bed. The contour of gas velocity magnitude (Fig. 12(a)) displays a variety of velocity streaks, ranging from low to high, which includes areas of stagnation as well as high-velocity channels that emerge in the narrow gaps between spheres. Furthermore, the presence of high-velocity magnitudes indicates a highly three-dimensional flow, characterized by rotational movements and curvature in the streamlines within the packed bed system. The maximum gas velocity of 0.71 m/s is found in the narrow gaps between the stacked spherical particles (Fig. 12(a)), leading to local increases in Reynolds number. The maximum Reynolds number in Section 1 is 280, which is a function of gas velocity and thermophysical properties (Fig. 12(b)). However, the locations of the maximum Reynolds number do not necessarily correspond to the locations of the largest gas velocity, as the thermophysical properties of air also affect the flow behavior. The Prandtl number varies slightly between 0.691 and 0.7 and can be considered approximately constant throughout the packed bed. To better understand the flow behavior in the axial direction, a quantitative analysis of the dimensionless velocity distributions along two lines, that is, line1 (in Section 1 and along the z direction, the coordinates of the starting point are ($0.5D_t$, 0, 0)), line2 (in Section 1 and along the z direction, the coordinates of the starting point are ($0.75D_t$, 0, 0)) are plotted. The positions of line1 and line2 are shown in Fig. 13. The data reveal significant velocity gradients within the pores, with local velocities in larger pore regions reaching up to 3.8 times the inlet velocity. It is important to note that velocity distribution is influenced by the location of the pores and temperature variations. Under the same mass flow rate, higher gas temperatures result in reduced gas density, thereby increasing the gas velocity.

Fig. 14 shows the velocity and temperature distributions in different cross-sections (Sections 2 and 3) of the randomly packed bed with uniform spheres. It can be observed that the gas velocity distribution is affected by the local structure within the packed beds, which in turn influences the temperature distribution of the gas, as shown in Fig. 14(a). The regions with higher gas velocity correspond to higher gas temperatures in Fig. 14(b), which further affects the temperature distribution of the solid particles as shown in Fig. 14(c). To analyze
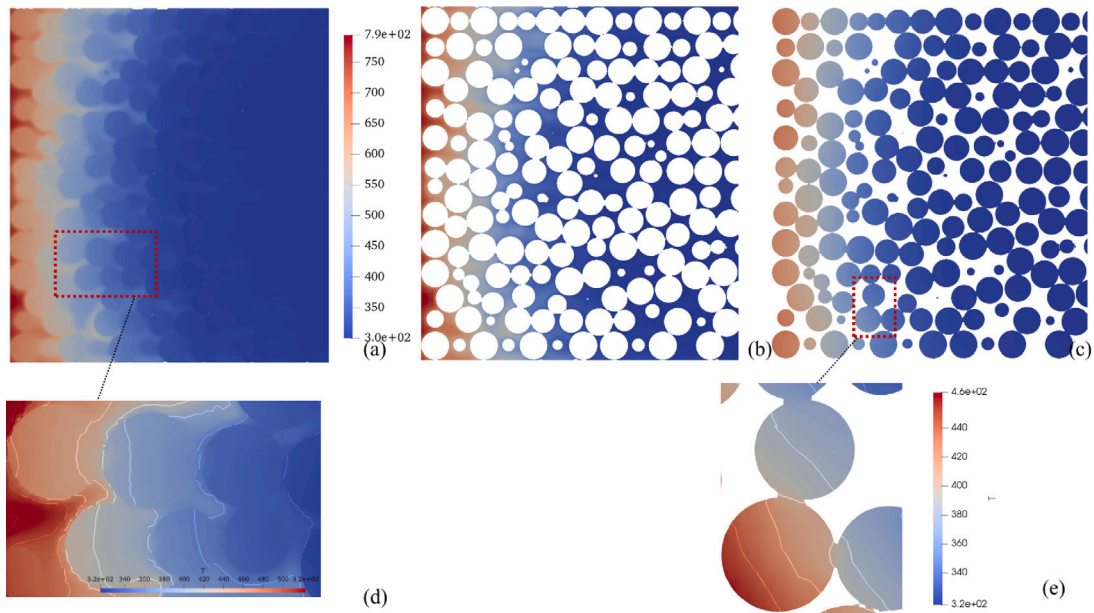
Fig. 11. Temperature fields in Section 1 of the randomly packed bed (u = 0.1 m/s, t = 1000 s). (a) Total temperature field (gas and solid), (b) Gas temperature field, (c) Solid temperature field, (d) Zoomed-in view of the temperature field at the gas-solid interface, (e) Zoomed-in view of the solid temperature field.
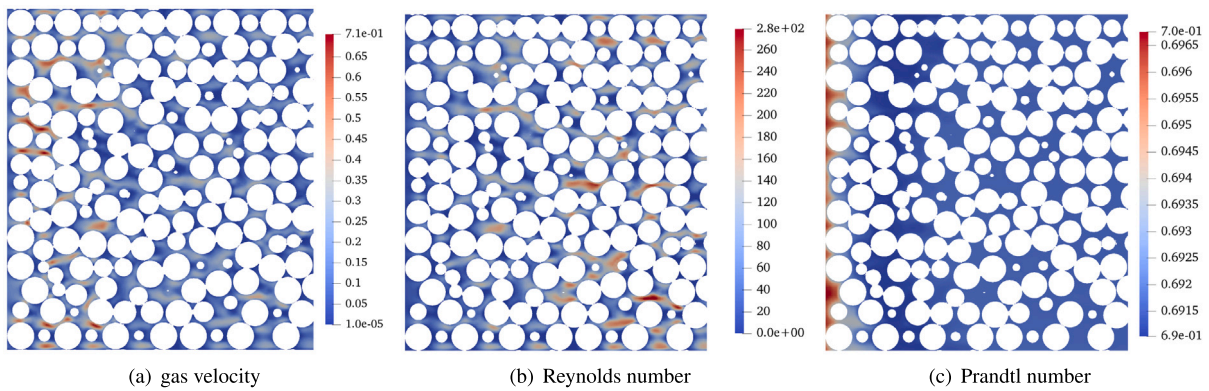

(a) gas velocity   (b) Reynolds number   (c) Prandtl number

Fig. 12. Gas velocity, Reynolds number, and Prandtl number distribution in Section 1 of the randomly packed bed with an inlet velocity of 0.1 m/s and a time of 1000 s.
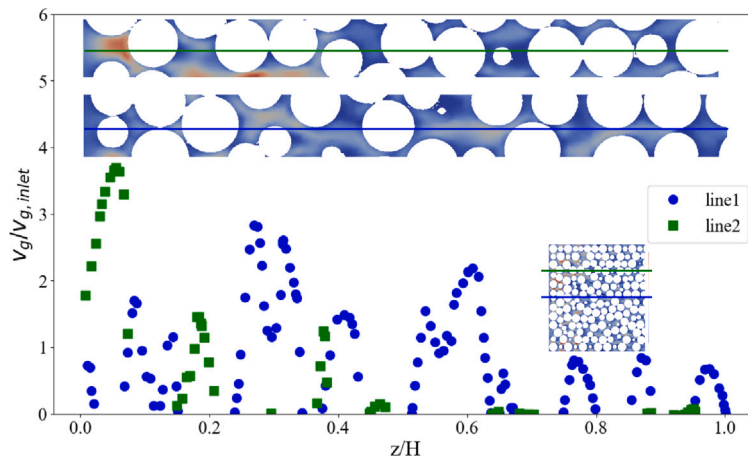
Fig. 13. Dimensionless velocity distributions on the two z-direction lines in Section 1.

further the three-dimensional flow characteristics, we plot the three components of the velocity field on one line, that is, line3 (in Section 2 and along the $-y$ direction, the coordinates of the starting point are ($0.5D_t$, 0 $0.1H$)). The positions of line3 are shown in Fig. 15. The velocity component's magnitude demonstrates instances of reverse flow (as indicated by negative velocities in Fig. 15). In the v_{g_y} components,

(a) gas velocity in section-2   (b) gas temperature in section-2   (c) solid temperature in section-2

(d) gas velocity in section-3   (e) gas temperature in section-3   (f) solid temperature in section-3
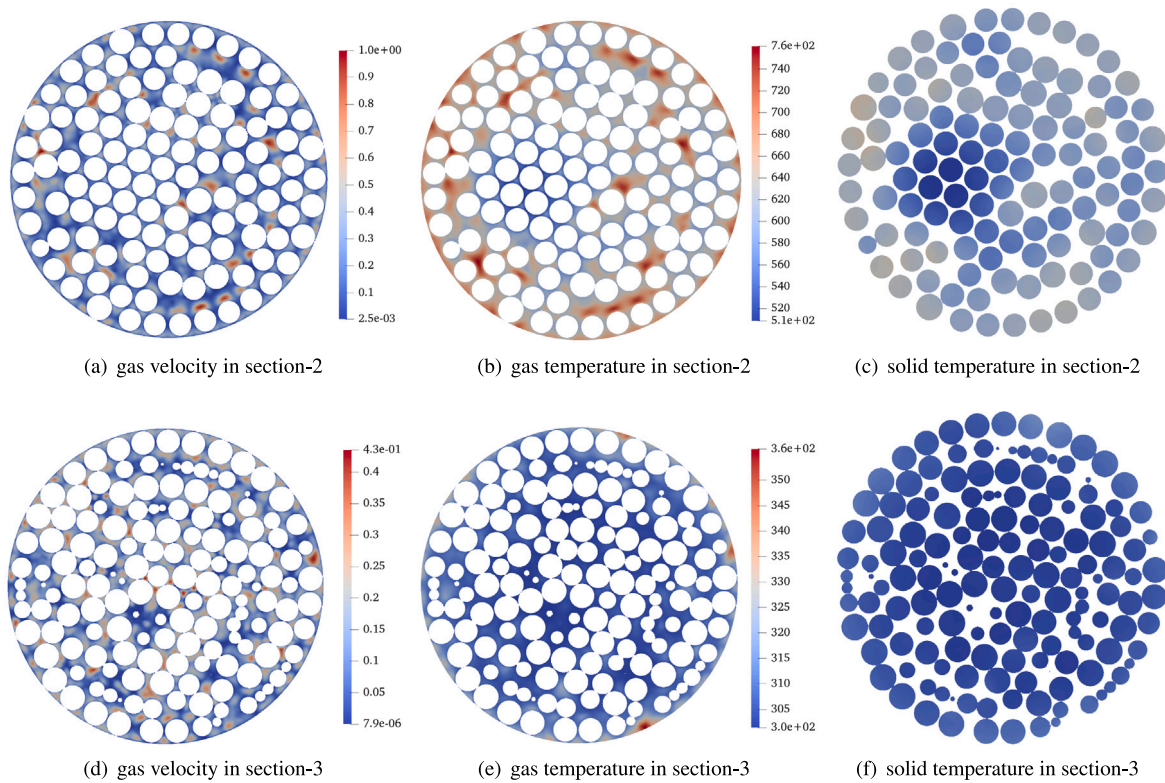
Fig. 14. Gas velocity (m/s) and temperature (K) distributions in different sections with an inlet velocity of 0.1 m/s and a time of 1000 s.
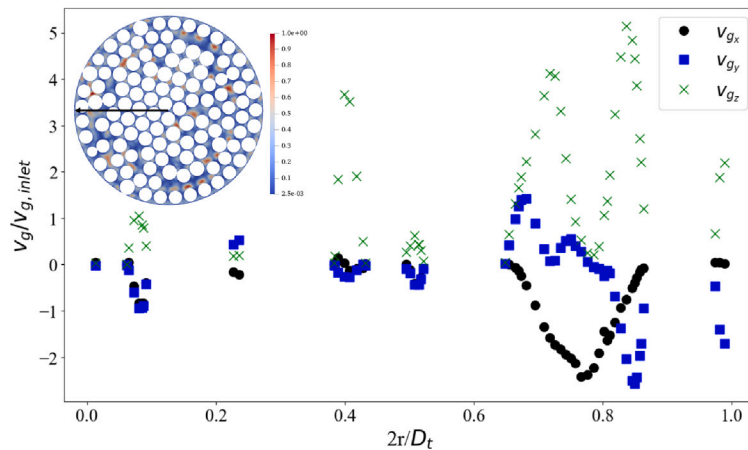
Fig. 15. Three components of the velocity field in line3, plotting from the center to the wall surface.

a transition between high and low-velocity zones is evident, indicating a strong cross-flow with highly three-dimensional flow characteristics in the bed. Fig. 14(d), (e), and (f) depict the distributions of gas velocity, gas temperature, and solid temperature in Section 3, which exhibit similar distribution patterns as those in Section 2. The analysis of internal heat conduction within individual solid particles has been carried out in Fig. 11 (Section 1).

3.2.2. Effect of gas velocity

The purpose of this Subsection is to analyze the influence of different inlet gas velocities on the volumetric heat transfer coefficient. First, we obtained the transient average temperature distribution of gas and solid for different inlet gas velocities. Then, by solving Eq. (1), we can determine the numerical values of h_v.

Fig. 16 presents the average temperature distribution of gas and solid inside the packed bed for different inlet velocities (0.01 to 0.5

m/s), which are represented by the Reynolds number (at room temperature). The temperature of gas and solid were averaged in the xy plane of the geometry, and their averages were plotted in the z-direction, where z/H = 0.1 and 0.7 correspond to Section 2 and Section 3 shown in Fig. 10. As the inlet velocity increases, both fluid and solid temperatures within the packed bed rise. This rise is attributed to the increase in flow velocity, which, during the simulated transient heat transfer process, allows the fluid to propagate further at the same moment. Moreover, the average temperature difference decreases with the increase of the inlet velocity at the same moment. This decrease is due to enhanced flow intensity, promoting better heat convection from pore areas to spherical surfaces and accelerating solid heating. Using Fig. 16(c) as an example, we observe a temperature difference ($dT = \overline{T_g} - \overline{T_s}$) of about 28 K between the average gas temperature and the average solid temperature in Section 2 plane (z/H = 0.1), while in Section 3 plane (z/H = 0.7), this value increases to 39
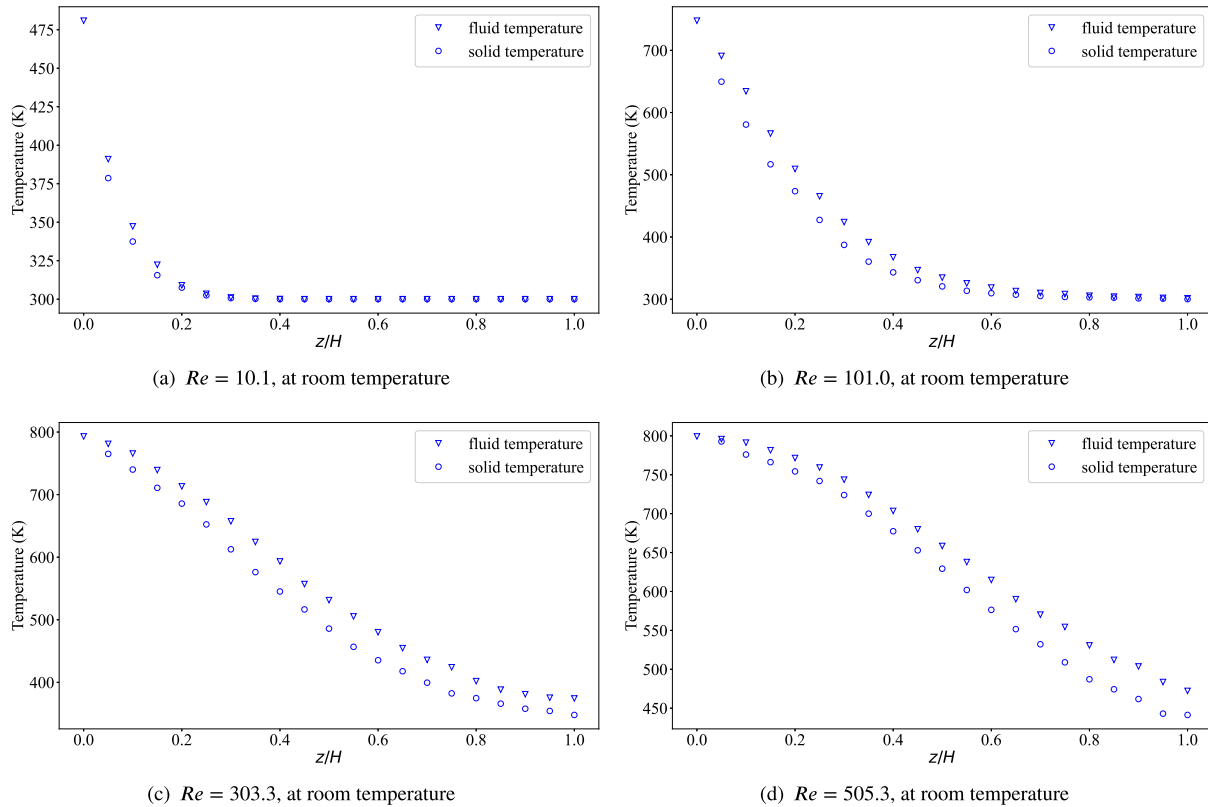
Fig. 16. Temperature fields comparison between fluid and solid phases at 1000 s. The fields are averaged in the xy plane of the packed bed and plotted along the z direction. Different inlet velocities are considered.

K, where $\overline{T_i}$ is the average temperature of the i-phase in each cross-section, $\overline{T_i} = \frac{1}{S_i} \int_{S_i} T_i dS$, with S_i being the area of the cross-section. These observations strongly suggest the existence of local thermal non-equilibrium (LTNE) during the transient heat transfer process, which is characterized by a temperature difference between the average gas and solid phases in the same plane. Furthermore, our analysis revealed that a higher Reynolds number leads to faster heating of the solid particles.

The volumetric heat transfer coefficient h_v is an important parameter in the analysis of heat transfer in packed beds, and it is influenced by transient changes in thermal conductivity k_g and average temperatures $\langle T_s \rangle^s$ and $\langle T_g \rangle^g$ over time, as defined in Eq. (1). Fig. 17 shows the predicted relationship between the heat transfer coefficient h_v and time for various inlet gas velocities. It is observed that h_v increases with time for all Reynolds numbers, but the rate of increase varies significantly. For low Re corresponding to inlet velocities such as 0.01 m/s and 0.1 m/s, the increase in h_v over time is relatively small, with around 2.7% and 1.5% increases, respectively, and therefore h_v can be regarded as constant. However, for Re of 505.3, h_v significantly increases with the heat transfer process, with an increase of about 42% from 10407.68 to 14827.37 W/(m^3 K). These findings suggest that Re has a significant impact on the heat transfer coefficient in packed beds, with higher Re resulting in a more significant increase in h_v over time.

3.2.3. Effect of solid thermal conductivity

To explain the temperature distribution behavior within the particles, the Biot number is introduced [25].

$$Bi = \frac{h_s d_{par}}{k_s} = \frac{h_v d_{par}^2}{6\varepsilon_s k_s} \quad (11)$$

where Bi is determined by both the volumetric heat transfer coefficient h_v and the solid thermal conductivity k_s. Note that $h_v = h_s A_s$, where A_s is the specific surface area which can be expressed as $A_s = A_{gs}/V =$

$6\varepsilon_s/d_{par}$. Bi depends on h_v, which depends on k_s. Therefore, k_s has to be set and Bi verified as a posterior.

The effect of the solid thermal conductivity k_s on the temperature distribution and heat transfer coefficient inside the packed bed was investigated. Four different values of k_s (0.1, 1, 10, and 100 W/(m K)) independent of the temperature were considered as a single variable, with a constant value that does not vary with temperature in each simulation.

The inlet gas velocity was set to a constant value of $|\langle v_g \rangle| = 0.3$ m/s ($Re = 303.3$ at room temperature) in all four simulations. Fig. 18 displays the solid temperature distribution in Section 2 for the different k_s values. Specifically, Fig. 18(a), (b), (c), and (d) correspond to k_s values of 0.1, 1, 10, and 100 W/(m K), respectively. The temperature contour intervals were set to 10 K for Fig. 18(a), b, and c, while for Fig. 18d, it was set to 5 K. As shown in Fig. 18(a), the temperature difference from the center of each sphere to the surface is nearly 80 K, indicating significant temperature non-uniformity within individual particles. Similarly, Fig. 18(b) shows a temperature difference of nearly 20 K. In both a and b cases, heat conduction within the sphere cannot be neglected. Conversely, in the latter two cases, where k_s values are 10 and 100 W/(m K), the temperature variation within individual particles is less than 10 K, implying that heat conduction inside the sphere can be neglected. This observation can also be confirmed by Fig. 18(c) and (d).

Fig. 19 presents the time-dependent increase in h_v for packed beds for different solid thermal conductivities, indicating that k_s affects the evolution of h_v. The results show that h_v increases gradually over time for all solid thermal conductivity values, but at a slower rate for lower solid thermal conductivity values. For example, in Fig. 19, for a solid thermal conductivity of 0.1 W/(m K), h_v increases by 12.9% from 4782.11 to 5403.18 W/(m^3 K), while for a solid thermal conductivity of 100 W/(m K), h_v increases by 27.4% from 7839.24 to 9989.57
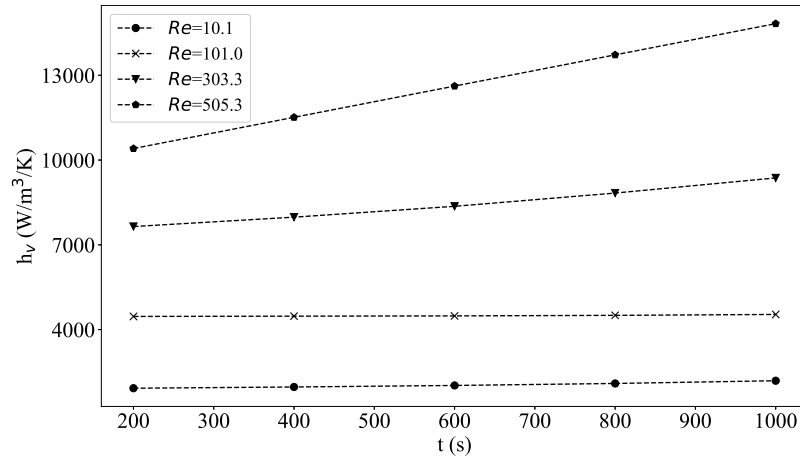
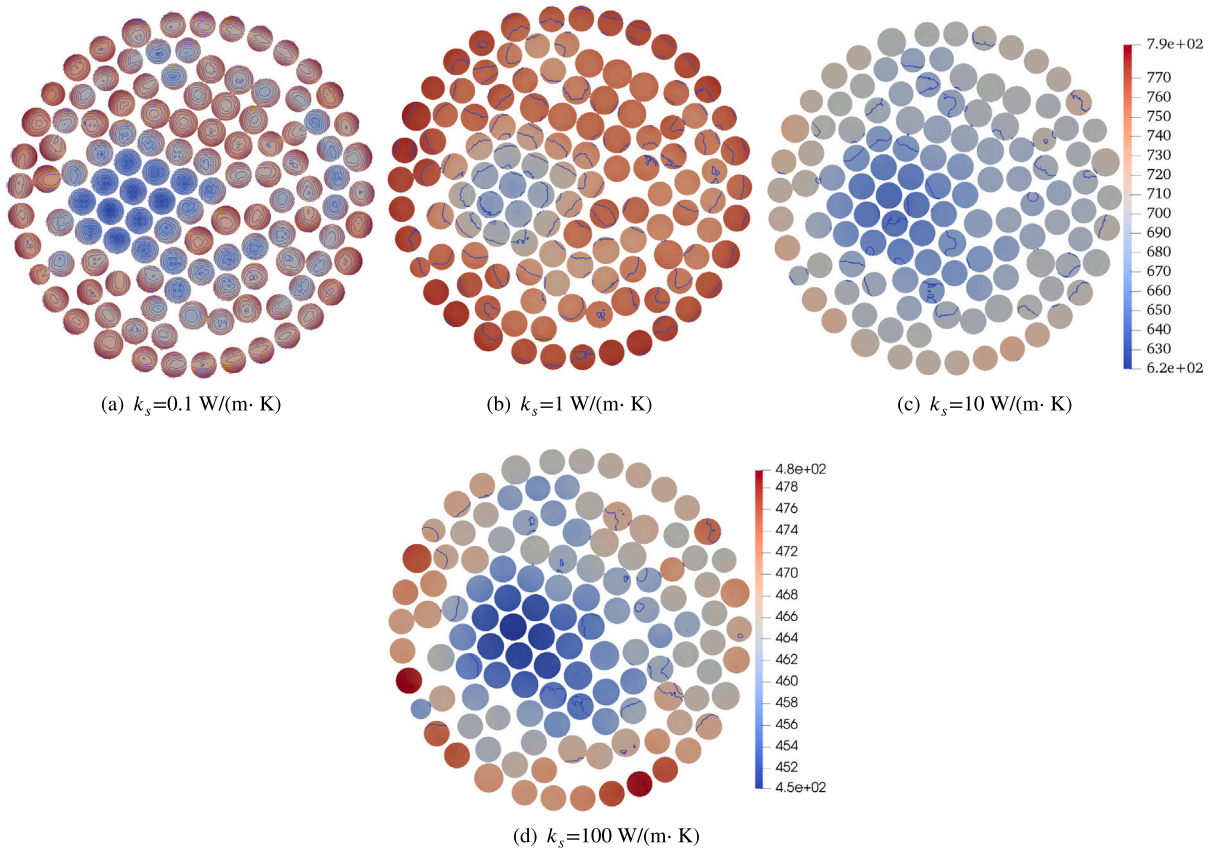**Fig. 17.** Transient behavior of heat transfer coefficient as a function of time for various inlet velocities.

(a) k_s=0.1 W/(m· K)   (b) k_s=1 W/(m· K)   (c) k_s=10 W/(m· K)

(d) k_s=100 W/(m· K)

Fig. 18. Solid temperature distribution at Section 2 for various solid thermal conductivity values.

W/(m^3 K). Furthermore, an increase in solid thermal conductivity k_s results in a corresponding increase in h_v at a given time.

The data presented in Fig. 19 indicates that an increase in the solid thermal conductivity k_s correlates with an increase in h_v for a fixed time. The Biot numbers calculated from Eq. (11), using h_v values at t = 1000 s, are 3.72, 0.62, 0.063, and 0.0069 for k_s values increasing from 0.1 to 100 W/(m K). This indicates that, at a specific time step, h_v increases with a decrease in Biot number. These values explain the temperature gradient behavior seen in individual particles in Fig. 18(a) and (b), where the Biot number is above 0.1. On the other hand, the

Biot numbers for Fig. 18(c) and (d) are below 0.1, showing that the temperature distribution within individual particles is uniform.

4. Numerical method and results at the macro-scale

This section aims to validate the effectiveness of the integral method presented in Section 3. The verification procedure consists of the following steps: Firstly, a simplified micro-scale geometry is generated, adopting the same porous structure as depicted in Fig. 3, but excluding the flow1 and flow2 regions. This approach is employed to eliminate the influence of boundary conditions applied at the interface between
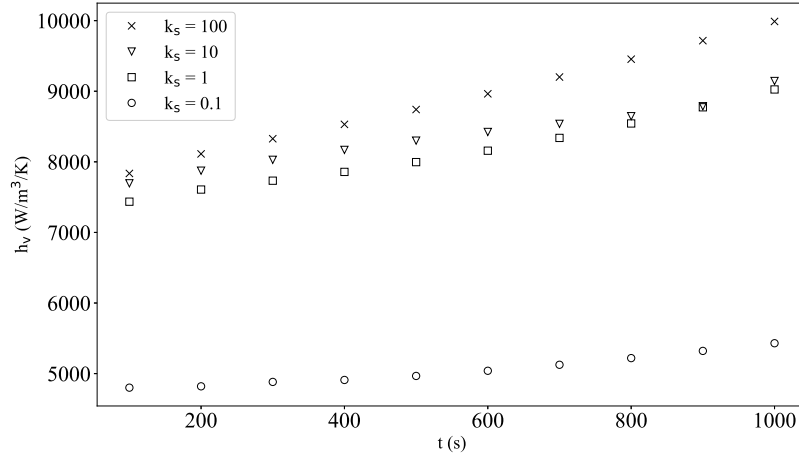
Fig. 19. Evolution of volumetric heat transfer coefficient h_v with time for packed beds with different solid thermal conductivities.

(a) Micro-scale domain

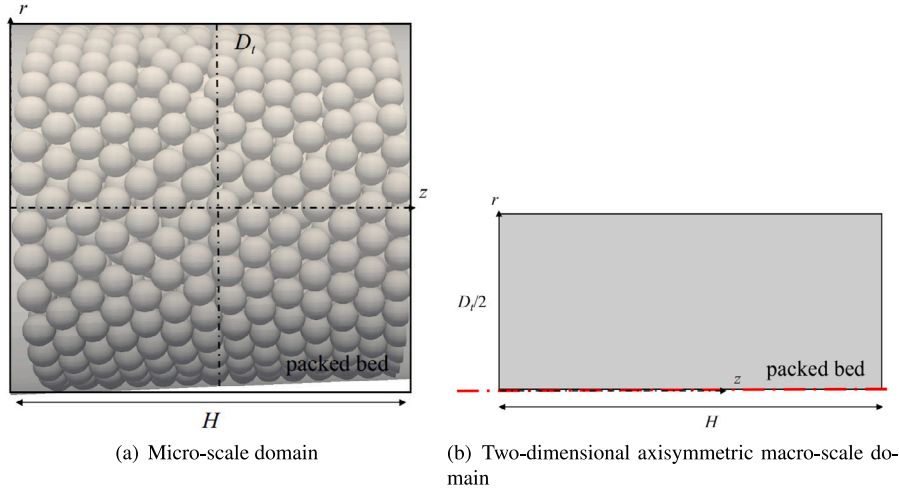(b) Two-dimensional axisymmetric macro-scale domain

Fig. 20. Numerical domains at micro and macro-scales.

the flow1 and packed bed regions. The resulting micro-scale model is presented in Fig. 20(a). The volumetric heat transfer coefficient h_v is calculated using the same integral method. Secondly, the macroscopic equations are solved using the derived parameters from the micro-scale simulation, and a comparison is made between the temperature fields in the micro-scale and macro-scale models.

4.1. Numerical model

To ensure a consistent comparison between simulation results at the macro and micro scales, it is crucial to maintain identical structures in both simulations. The micro-scale structure, depicted in Fig. 20(a), consists exclusively of the packed bed region. In the macro-scale simulation, a two-dimensional axisymmetric numerical domain, as shown in Fig. 20(b), is utilized. By maintaining this consistency in structure, accurate and reliable comparisons can be made between the macro and micro scales.

4.1.1. Mathematical model and numerical implementation

For the porous domain (packed bed), we employ the LTNE model. The Reynolds number, based on the particle diameter (d_{par}), is defined as $Re = \rho_g |\langle v_g \rangle| d_{par} / \mu_g$, with $|\langle v_g \rangle|$ being the average gas velocity. As mentioned in Section 3, the Reynolds number ranges from 10.1

to 505.3, indicating that the gas flow is in the Forchheimer flow regime. Therefore, we use the Forchheimer equation in the macroscopic simulation. The averaged governing equations can be expressed as follows [57]:

$$\frac{\partial}{\partial t}\left(\varepsilon_g \frac{M\langle p\rangle^g}{R\langle T_g\rangle^g}\right) + \nabla \cdot \left(-\frac{M\langle p\rangle^g \mathbf{K}\mathbf{X}}{R\langle T_g\rangle^g}\cdot \nabla\langle p\rangle^g\right) = 0 \tag{12}$$

$$\frac{\partial}{\partial t}\left(\varepsilon_s \rho_s c_{p,s}\langle T_s\rangle^s\right) = \nabla \cdot (\mathbf{k_{s,eff}}\cdot \nabla\langle T_s\rangle^s) + h_v\left(\langle T_g\rangle^g - \langle T_s\rangle^s\right) \tag{13}$$

$$\frac{\partial}{\partial t}\left(\varepsilon_g \rho_g c_{p,g}\langle T_g\rangle^g\right) + \nabla \cdot (\rho_g c_{p,g}\langle \mathbf{v_g}\rangle^g\langle T_g\rangle^g) = \nabla \cdot (\mathbf{k_{g,eff}}\cdot \nabla\langle T_g\rangle^g)$$
$$+ h_v\left(\langle T_s\rangle^s - \langle T_g\rangle^g\right) \tag{14}$$

where Eq. (12) represents the gas mass conservation equation, which is derived from the ideal gas law (Eq. (15)), mass conservation (Eq. (16)), and Forchheimer equation (Eq. (17)). Eqs. (13) and (14) are the energy equations for the solid and fluid phases, respectively.

$$\rho_g = \frac{M\langle p\rangle^g}{R\langle T_g\rangle^g} \tag{15}$$

$$\partial_t \left(\varepsilon_g \rho_g\right) + \nabla \cdot \left(\varepsilon_g \rho_g \langle \mathbf{v_g}\rangle^g\right) = 0 \tag{16}$$

$$\langle \mathbf{v_g}\rangle^g = -\frac{1}{\varepsilon_g}(\mathbf{K}\mathbf{X})\cdot \nabla\langle p\rangle^g, \quad X_{ij} = \frac{1}{\mu_g K_{ij} + \beta_{ij}\rho_g |\langle v_g\rangle|} \tag{17}$$

Table 6
Initial and boundary conditions of the LTNE model.

Region	Initial conditions		Boundary conditions		
packed bed		inlet	lateral boundaries	outlet	
$\langle p \rangle^g$	101 325 Pa	*forchheimer Velocity Pressure*	*zero gradient*	*fixed value* (101 325 Pa)	
$\langle T_g \rangle^g$	300 K	*fixed value* (800 K)	*zero gradient*	*zero gradient*	
$\langle T_s \rangle^s$	300 K	*zero gradient*	*zero gradient*	*zero gradient*	

where the Forchheimer tensor, represented as **X**, is introduced to simplify the computation process [58]. Considering the packed bed as isotropic allows us to treat **K** and β as scalars. This implies that $\mathbf{K} = K\mathbf{I}$ and $\beta = \beta\mathbf{I}$, where **I** is the identity tensor. The averaged governing equations presented in Eqs. (12), (13), and (14) have already been validated against experimental results in a previous work [48].

In what follows, $\langle T_g \rangle^g$ and $\langle T_s \rangle^s$ correspond to the gas and solid temperatures in the porous domain (packed bed). The boundary conditions and initial conditions for the system of Eqs. (13) and (14) (LTNE model) are specified in Table 6. For the pressure, the *forchheimer Velocity Pressure* condition provides a compressible Forchheimer's velocity condition for pressure. It is derived from a *fixed Gradient* condition, whereas pressure is calculated from the projection of the velocity vector and permeability tensor on the direction of the flow.

The numerical model was implemented using the finite volume method in the Porous material Analysis Toolbox based on OpenFOAM (PATO) [59], which is available in open access. For the porous domain, the pressure equation (Eq. (12)) was solved semi-implicitly using first-order schemes in time (Euler) and space (Gauss linear). The pressure gradient term was implicit, while the other terms were explicit. The same approach was used for the energy equations, where the temperature terms were implicit and the other quantities were explicit. The equations were solved in series, with appropriate mesh refinement and time steps to ensure convergence.

4.1.2. Physical properties

The parameters mentioned in the averaged governing equations (Eqs. (12), (13), (14)), including permeability **K**, Forchheimer coefficient β (Eq. (17)), porosity ε_g, gas properties ($\rho_g, \mu_g, c_{p,g}, k_g$), and solid properties ($k_s, c_{p,s}, \rho_s$), were obtained from the micro-scale simulations and are summarized as follows. The values of K and β are listed in Table 5, the value of ε_g is 0.379, and the thermal properties of gas and solid are presented in Table 4. For the effective parameters, including the effective solid thermal conductivity $\mathbf{k_{s,eff}}$, effective gas thermal conductivity $\mathbf{k_{g,eff}}$, and volumetric heat transfer coefficient h_v, we introduce several dimensionless coefficients, denoted as c_1, c_2, c_3 and f, as defined in Eq. (18), to facilitate the optimization algorithm. As presented in the introduction, the value of $\mathbf{k_{g,eff}}$ is influenced by the conductivity, tortuosity and dispersion terms, which exhibit different values in the longitudinal ($\parallel$) and transverse ($\perp$) flow directions [7,21]. The tortuosity term is typically neglected when compared to the dispersion term [60]. The relationship between the dispersion terms and the thermal properties of the gas follows a similar functional form as proposed by Wakao et al. [21]. Similarly, the modeling of h_v employs the same functional form as suggested by Wakao et al. [20].

$$
\begin{cases}
\mathbf{k_{s,eff}} = \mathbf{k_{s,con}} + \mathbf{k_{s,tor}} = c_1 \cdot k_s I \\
k_{g,eff,\parallel} = k_{g,con} + k_{g,tor,\parallel} + k_{dis,\parallel} = \varepsilon_g k_g + 0 + c_2 \cdot Re \cdot Pr \cdot k_g = \varepsilon_g k_g \\
\quad + c_2 \cdot d_{par} \cdot |\langle v_g \rangle| \cdot \rho_g \cdot c_{p,g} \\
k_{g,eff,\perp} = k_{g,con} + k_{g,tor,\perp} + k_{dis,\perp} = \varepsilon_g k_g + 0 + c_3 \cdot Re \cdot Pr \cdot k_g = \varepsilon_g k_g \\
\quad + c_3 \cdot d_{par} \cdot |\langle v_g \rangle| \cdot \rho_g \cdot c_{p,g} \\
h_v = (6\varepsilon_s/d_{par}) \cdot (2 + f \cdot Re^{0.6} \cdot Pr^{1/3}) k_g / d_{par}
\end{cases}
$$

$$(18)$$

where h_v is calculated using the Nusselt number, $Nu\ (= \frac{h_s d_{par}}{k_g} = \frac{h_v d_{par}^2}{6\varepsilon_s k_g})$, in the following expression: $Nu = 2 + f \cdot Re^{0.6} \cdot Pr^{1/3}$ [20], Prandtl number, Pr, is given by $Pr = \mu_g c_{p,g}/k_g$.

4.2. Optimization process and methods

An inverse analysis method was employed to determine the effective parameters by minimizing the errors between the predicted data from micro-scale simulations and the macro-scale results. In the subsequent analysis, T_g and T_s refer to the gas and solid temperatures obtained at the micro-scale, while $\langle T_g \rangle^g$ and $\langle T_s \rangle^s$ represent the gas and solid temperatures obtained at the macro-scale. Additionally, $\overline{T_g}$ and $\overline{T_s}$ denote the average temperatures obtained from the micro-scale simulations. We obtained data sequences, denoted as $\{\overline{T_{g,i}}\}_{i=1}^n$, and $\{\overline{T_{s,i}}\}_{i=1}^n$, which represent the average gas and solid temperatures at different cross-sections indicated by the index i. The cross-sections are evenly spaced at intervals of $0.05H$ along the packed bed, ranging from $z = 0$ to $z = H$ (as presented in Fig. 20(a)). These data sequences were collected at three distinct time points: $t = 300$ s, $t = 500$ s, and $t = 1000$ s, a total of 6 data sequences. The error function S over the six sequences is [32]

$$
S = \frac{1}{6} \left(\sqrt{\frac{1}{n} \sum_{i=1}^{n} \left(\frac{\langle T_{g,i} \rangle^g - \overline{T_{g,i}}}{\overline{T_{g,i}}} \right)^2} + \sqrt{\frac{1}{n} \sum_{i=1}^{n} \left(\frac{\langle T_{s,i} \rangle^s - \overline{T_{s,i}}}{\overline{T_{s,i}}} \right)^2} \right)_{t=300s,500s,1000s}
$$

$$(19)$$

The minimization of S was performed using the Design Analysis Kit for Optimization and Terascale Applications (DAKOTA) [61]. The local optimization method employed was the Adaptive Nonlinear Least-Squares Algorithm (NL2SOL) [62]. NL2SOL utilizes a quasi-Newton update approach to quickly estimate the optimal value. By approximating the Hessian matrix using a simplification scheme, NL2SOL achieves faster convergence compared to global optimization methods for least squares calculations. An overview of the optimization process is presented in Fig. 21. A detailed description of this optimization strategy can be found in the next section.

4.3. Simulation results at the macro-scale

In this subsection, we present the results of predicted temperatures obtained from micro-scale and macro-scale simulations. Fig. 22 provides a comparison between these two scales at three different time points: $t = 300, 500, 1000$ s. The micro-scale results ($\overline{T_g}$ and $\overline{T_s}$) are represented by data points, while the macro-scale results ($\langle T_g \rangle^g$ and $\langle T_s \rangle^s$) are shown as continuous lines. Specific markers and line styles distinguish each time point. The blue color corresponds to the gas phase and the black color for the solid-phase. The procedure for determining the effective parameters is then presented.

Based on the model presented in Section 4.1.2, there are four parameters to optimize: c_1, c_2, c_3, and f. Studies [60] have indicated that the maximum value of effective gas thermal conductivity in the transverse flow direction, $k_{g,eff,\perp}$, is 0.4 $\varepsilon_g k_g$ when the maximum Peclet number ($Pe = Re \cdot Pr$) is 300 in the packed bed. Similarly, the maximum value of effective gas thermal conductivity in the horizontal direction, $k_{g,eff,\parallel}$, is 250 $\varepsilon_g k_g$ under the same conditions. However, the

Table 7
The value of c_1, c_2, f and error S for different inlet gas velocities.

Re (at room temperature)	50.5	101.0	303.3	505.3
c_1	0.75 ± 0.03	0.75 ± 0.03	0.77 ± 0.03	0.77 ± 0.03
c_2	0.05 ± 0.005	0.09 ± 0.005	0.25 ± 0.02	0.28 ± 0.04
f	1.1 ± 0.04	1.2 ± 0.05	1.2 ± 0.05	1.2 ± 0.05
S	1.97×10^{-3}	1.94×10^{-3}	1.92×10^{-3}	1.92×10^{-3}
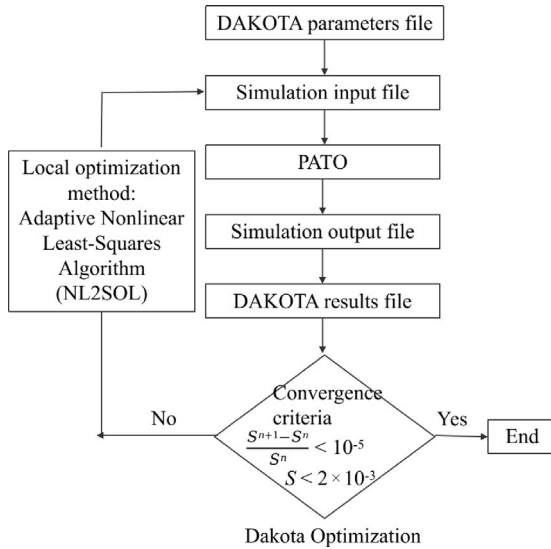
Fig. 21. The steps of optimization process.

influence of $k_{g,eff,\perp}$ is relatively small compared to $k_{g,eff,\parallel}$. Therefore, for the subsequent analysis, we set the value of c_3 to zero and focus on optimizing the remaining three parameters: c_1, c_2, and f.

To optimize the parameters, a representative case with $Re = 505.3$ (at room temperature) from our extensive simulations was selected. Additional case results are presented in Appendix C. To determine suitable ranges for the parameters, we consulted the existing literature and sought orders of magnitude. Based on the correlations proposed by Degrot et al. [60] for packed beds, we estimated the dispersion term c_2 to be around 0.31, and the effective solid thermal conductivity term c_1 was set to a simple form of ε_s, 0.621 for a Peclet number of 300. For the coefficient f, we chose the original form of the Wakao correlation [20] and assumed $f = 1.1$. Taking advantage of the local optimization ability of the NL2SOL algorithm, the following parameter ranges were defined: c_1 from 0.2 to 1.2, c_2 from 0 to 0.5, and f from 0.4 to 1.7. These ranges allow for a comprehensive search for the optimal parameter values. Convergence ($S < 0.002$) was reached after 89 iterations of the local optimization algorithm.

Fig. 23 presents the impact of the three variables (f, c_1 and c_2) on the error S. The grey scale in Fig. 23(a) represents the value of f, while the size of the points corresponds to the magnitude of S. As shown in Fig. 23(a), when S is below 0.002, the values of c_1 are concentrated around 0.77 with an uncertainty of $\pm$ 0.03, c_2 concentrates around 0.28 with an uncertainty of $\pm$ 0.04, The values of f range from 0.7 to 1.5. To further examine the error's response to changes in f, we fixed c_1 at 0.77 and c_2 at 0.28, varying only f as the input. As Fig. 23(b) displays, S first decreases and then increases. The lowest error, S, occurs at $f = 1.2$, with an uncertainty $\pm$ 0.05. To sum up, when the error S converges to the level of 2×10^{-3}, the ranges of the effective parameters from the optimization solution are given in Table 7. When considering the temperature dependency of the gas and solid thermal

properties, the coefficient c_1, which is related to the solid phase volume fraction ε_s (as shown in Eq. (18)), is found to increase from 0.621 to 0.75 for $Re = 50.5$ and 101.0, and 0.77 for $Re = 303.3$ and 505.3 (at room temperature). This value remains relatively constant across different Re. The coefficient c_2, associated with gas dispersion, shows an increasing trend with higher inlet velocities and is therefore not constant. The coefficient f increases from 1.1 to 1.2 compared to the original Wakao correlation (1.1) [20]. To gain a deeper understanding, the transient heat transfer coefficient results are now presented.

Fig. 24 presents the values of h_v obtained at both the micro and macro scales, along with their corresponding average temperatures at specific time points. In Fig. 24(a), we plot the transient variation of h_v at different inlet velocities. At the micro-scale, h_v represents the average value over the entire volume, as described by Eq. (1). Meanwhile, at the macro scale, where h_v is dependent on time and position within the packed bed, we calculate the average values using the "Integrate Variable" filter in Paraview to obtain the results. The results reveal that the discrepancy between the micro-scale and macro-scale h_v values is less than 3.8%, with the maximum difference occurring at the highest Re. Furthermore, Fig. 24(b) shows the average gas temperature $\langle T_g \rangle^g$ across the entire volume in the macro-scale simulation, providing a comprehensive view of the temperature variations.

To further investigate the overall behavior of the temperature in the packed beds, color maps of the simulation results at the macro scale are now presented. Fig. 25 shows the temperature fields within the packed bed region at 1000 s. Due to the imposition of a *zero gradient* boundary condition on the lateral boundaries for both gas and solid temperatures, they exhibit a one-dimensional variation only in the longitudinal direction. It is evident that there is a temperature difference between the local average gas and solid temperatures $\langle T_g \rangle^g$ and $\langle T_s \rangle^s$. The temperature difference ranges from 5 K to 27 K, indicating significant local thermal imbalances between the gas and solid phases. This occurs when the volumetric heat transfer coefficient, h_v, falls within the range of 11735.41-13940.27 W/(m$^3 \cdot$ K), suggesting local thermal non-equilibrium.

4.4. Microscopic analysis

As shown in Fig. 26, a (60 mm^3) cube was extracted from the entire packed bed structure. Within this cube, the XZ plane at the center was chosen for detailed observation, with its position presented in the lower right corner of Fig. 26. Sphere contours are indicated by blue solid lines. This small plane was selected to showcase the distributions of velocity and temperature, illustrating the influence of micro-level data on macro-level behavior, such as the local microstructure's effect on macroscopic flow and heat transfer phenomena.

Fig. 27 shows the gas velocity variation at $t = 1000$ s, with the velocity field exhibiting high-speed regions in narrow gaps between spheres at different Reynolds numbers. The flow direction is from left to right. At a lower Reynolds number ($Re = 10.1$), the flow is smooth with a uniform velocity distribution and fewer high-velocity areas, indicating a steady passage of fluid through the gaps and more pronounced stagnation regions. As the Reynolds number increases ($Re = 101.0$), the velocity distribution becomes more uneven, suggesting an enhanced dynamic interaction between the fluid and the sphere surfaces and the formation of faster flow streaks. At the highest Reynolds
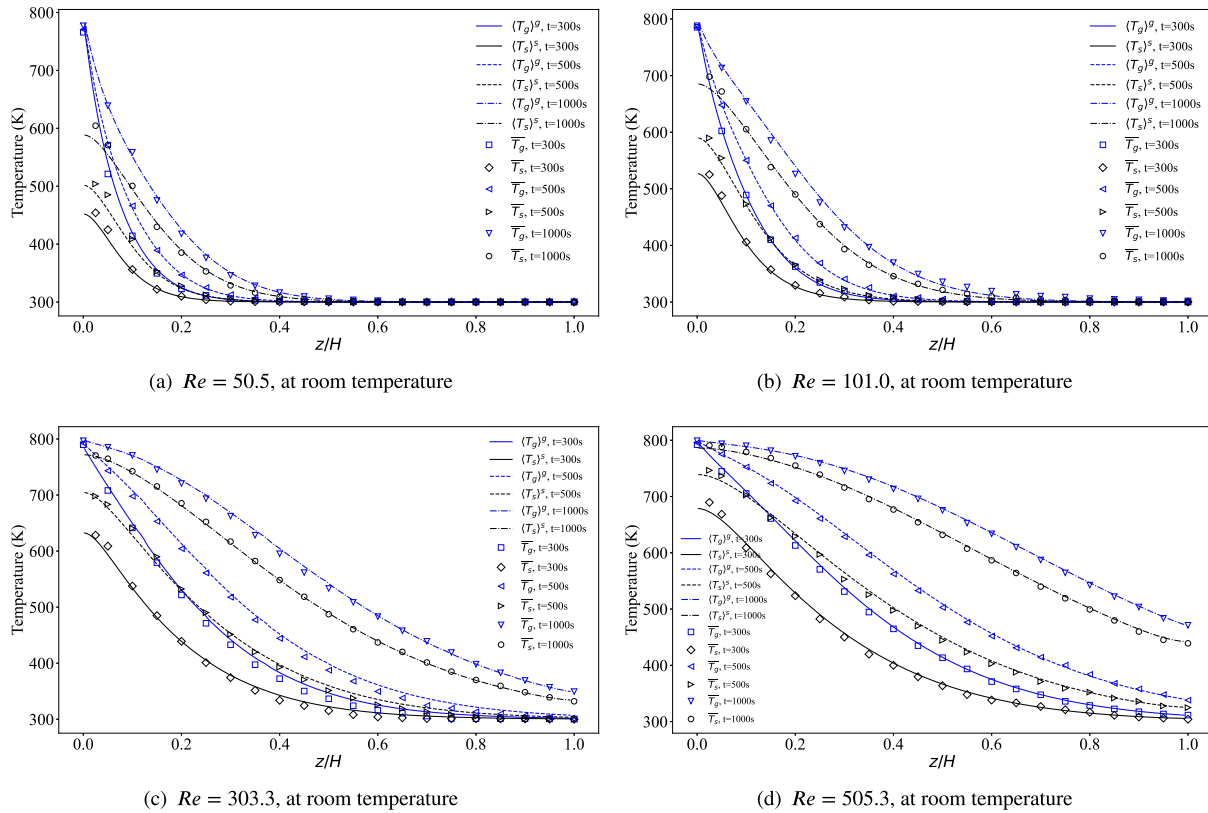
(a) $Re = 50.5$, at room temperature

(b) $Re = 101.0$, at room temperature

(c) $Re = 303.3$, at room temperature

(d) $Re = 505.3$, at room temperature

Fig. 22. Computed temperature field evolution in macro-scale and micro-scale with increasing inlet gas velocity by inverse analysis.

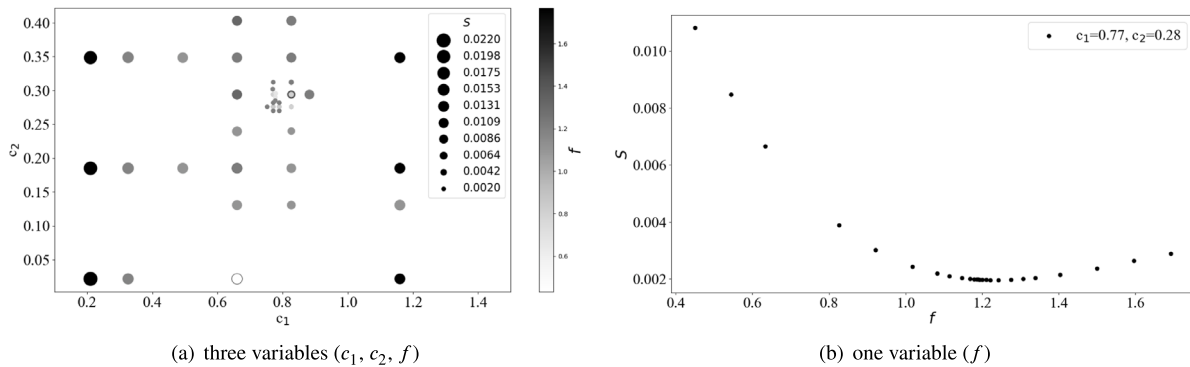(a) three variables (c_1, c_2, f)

(b) one variable (f)

Fig. 23. The influence of the three variables c_1, c_2, f on the error S, $Re = 505.3$.

number examined ($Re = 303.3$), the variations in velocity are more marked, with forced convection becoming the dominant factor [63]. As mentioned in Section 3.2.1, fluid motion within the packed bed is three-dimensional. Fig. 28 displays the three components of the gas velocity at $Re = 101.0$ on the selected plane ($t = 1000$ s). The velocity field reveals regions of reverse flow, as evidenced by negative velocities, and an alternation between high and low-velocity zones in both the $X-$ and $Y-$ components. This shows the presence of strong cross-flow within the bed.

The description of temperature variation in the domain shown in Fig. 29 follows an expected trend, starting with high temperatures on the left side due to the injection of hot gas. At a Reynolds number of $Re = 10.1$, distinct regions of high and low temperatures reflect sharp

gradients, indicating limited thermal spread influenced by the flow velocities. As the Reynolds number increases, the hot region expands, suggesting more effective convective heat transport. At the highest analyzed Reynolds number ($Re = 303.3$), the temperature distribution becomes more uniform, with the distinction between hot and cold regions becoming less pronounced, implying that convection is the predominant mechanism. Higher flow rates facilitate heat transfer to the cooler spheres, resulting in a balanced temperature field across the domain. Although the plane shown in Fig. 26 represents a localized area, the distribution of velocity and temperature fields allows us to see the effects of varying conditions on these physical quantities. Employing an integration method as shown in Eq. (1), we can derive

(a) Transient variation of h_v (b) Average local gas temperatures
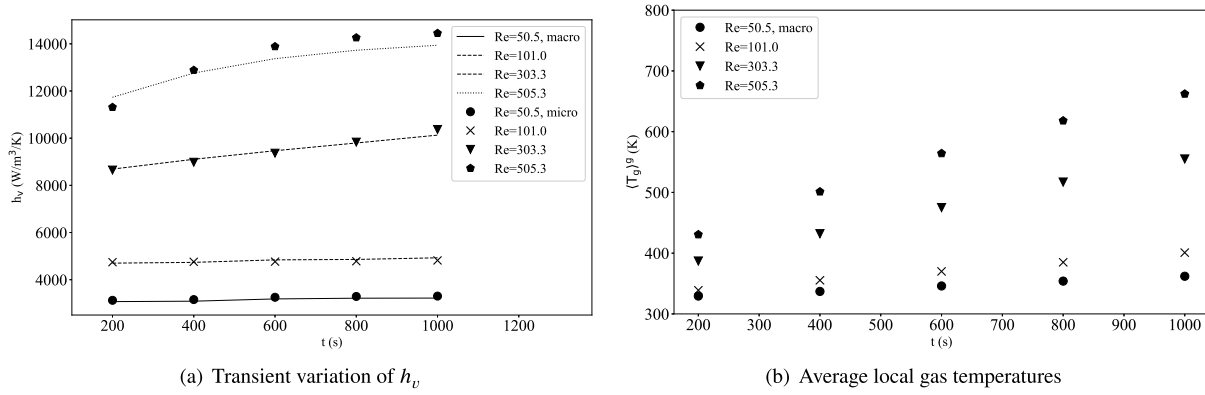
Fig. 24. Transient behavior of volumetric heat transfer coefficient and average local gas temperatures.

(a) gas temperature $\langle T_g \rangle^g$ (b) temperature difference between gas and solid $\langle T_g \rangle^g$-$\langle T_s \rangle^s$
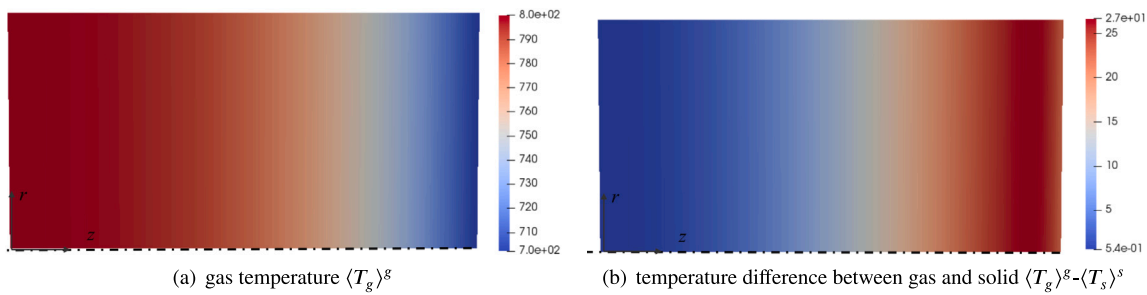
Fig. 25. Macroscopic gas temperature and the difference $\langle T_g \rangle^g$-$\langle T_s \rangle^s$ (K) in the packed bed region.
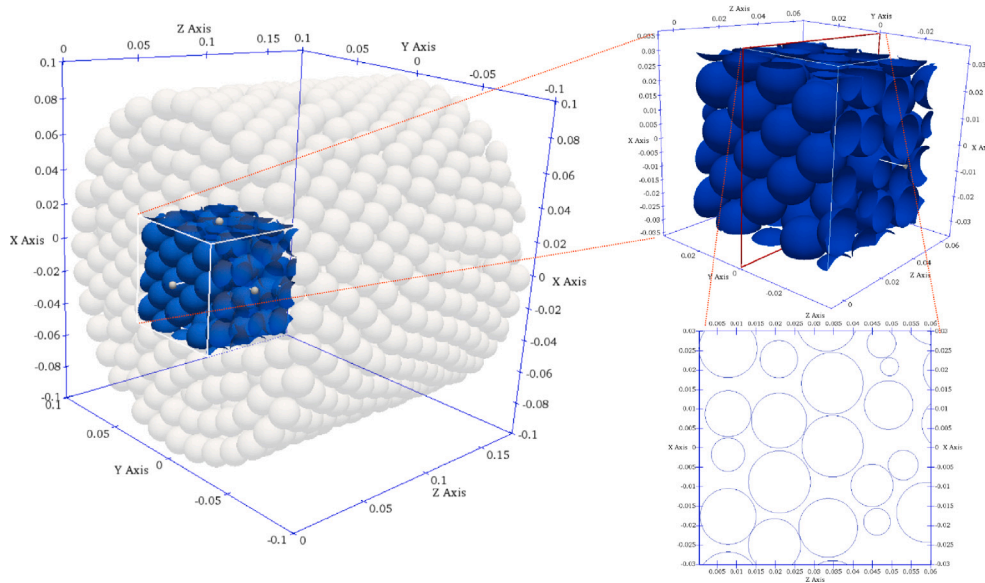

Fig. 26. Schematic location of the analyzed area.

macroscopic parameters, that is, the volumetric heat transfer coefficient. This parameter can reflect the impact of micro-level data on the macro-scale behavior.

Lastly, a fundamental comparison is provided regarding geometry generation, meshing, and run-time for both micro- and macro-scale simulations. In the micro-scale simulation, the first step involves generating the packed bed using a DEM code. Various simulation parameters, such as particle gravity, friction forces, and Poisson's ratio, must be taken into consideration. The generation process, executed on a single thread (Intel Core CPU i9-13900K @ 3.00 GHz, RAM 32 GB 4400 MHz), consumes around 10 h of computational time. Next, CFD tools from the OpenFOAM library (*snappyHexMesh*), are employed to mesh both the fluid and solid domains. To meet the computational demands, a portion of the MCIA cluster is utilized, comprising 4 nodes with 32 cores each (Intel Xeon Gold SKL-6130 @ 2.1 GHz) and 92 GB of RAM per node. The meshing process requires 8 h to complete.

- The volumetric heat transfer coefficient h_v was directly calculated from micro-scale field data through numerical integration of thermal fluxes between phases. Although h_v exhibited a transient behavior, it remains relatively stable at lower Reynolds numbers (e.g., 10.1 and 101.0). However, at a higher Reynolds number (e.g., 505.3), h_v significantly rises over time, showing a 42% increase from 10407.68 to 14827.37 W/(m³ K).
- The comparison between the h_v value obtained through the integration of micro-scale results and the one calculated from the inverse analysis revealed a discrepancy of less than 3.8%, with the maximum difference occurring at the highest Re. This indicates that the use of an inverse analysis to determine the volumetric heat transfer coefficient is a reliable method for cases similar to the ones treated in this work.

This study successfully connected simulations at the micro-scale and at the macro-scale, providing a comprehensive understanding of flow and heat transfer coefficients from a multi-scale perspective.

CRediT authorship contribution statement

Shaolin Liu: Investigation, Software, Writing – original draft, Writing – review & editing. **Azita Ahmadi-Senichault:** Supervision, Validation, Writing – review & editing. **Victor Pozzobon:** Writing – review & editing. **Jean Lachaud:** Writing – review & editing, Writing – original draft, Supervision, Software, Formal analysis.

Declaration of competing interest

The authors declare that they have no known competing financial interests or personal relationships that could have appeared to influence the work reported in this paper.

Data availability

Data will be made available on request.

Acknowledgments

Appendix A. Verification of gravity's influence

To confirm the impact of gravity, we calculated some dimensionless numbers, such as the Grashof number (Gr), and the Richardson number (Ri) [64]. The intensity of natural convection in the packed bed depends mainly on the Grashof number (Gr) with the spherical diameter (d_{par}) as the characteristic scale. The intensity comparison between natural and forced convection in mixed convection is mainly reflected by the Richardson number (Ri). The Grashof number (Gr) and Richardson number (Ri) in packed beds are defined as follows [64–66].

$$Gr = \frac{g\omega\Delta T d_{par}^{3}}{v_g^{2}}, \qquad Ri = \frac{Gr}{Re^2} \qquad (20)$$

where g is the acceleration due to gravity, ω is the coefficient of volume expansion (equal to approximately $1/T$ for ideal gases), ΔT is the temperature difference between the particles and the heat transfer fluids, v_g is the kinematic viscosity of the gas. Taking an inlet velocity of 0.1 m/s as an example, the Reynolds number is 101.0. In the Grashof number formula, the value of g is 9.8 m/s², the coefficient of thermal expansion ω is approximately 0.002 K⁻¹ (The temperature is set to the gas's average temperature, 500 K), the temperature difference ΔT is 15 K, the particle diameter d_{par} is 0.016 m, and the kinematic viscosity of the gas v_g is 3.7×10^{-5} m²/s. Upon calculation, the Grashof

Table 8
Values of the Richardson number in different cases.

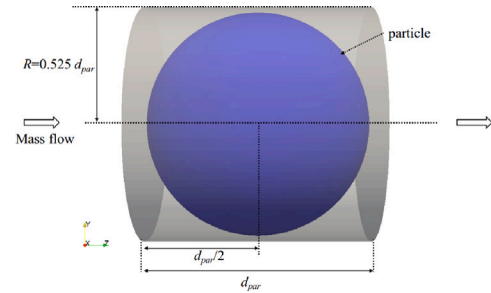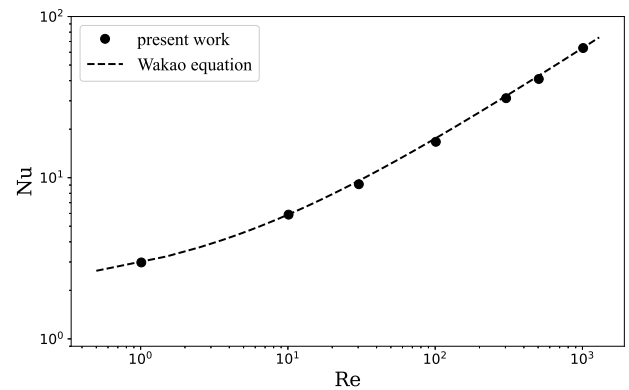| Dimensionless number				
Reynolds number (Re)	10.1	101.0	303.3	505.3
Grashof number (Gr)	912.4	879.6	741.1	360.5
Richardson number (Ri)	8.9	0.09	0.008	0.001

Fig. 30. Physical model used by Wakao.

Fig. 31. Variations of Nusselt number as a function of Reynolds number for the present simulation and Refs.

number is 879.6, and the Richardson number is 0.09. The values of these dimensionless numbers across different cases are summarized in Table 8. By definition, if the Richardson number is much less than one, natural convection may be neglected [65,67]. Given that in our cases, most of the Richardson numbers are much less than one, our assumption that the effects of gravity can be ignored is justified.

Appendix B. Micro-scale model validation

To ensure the accuracy of the present numerical model, the heat transfer process in the structure with the working conditions identical to an experiment carried out by Wakao et al. [51] has been simulated [68]. Fig. 30 presents the physical model used by Wakao. In this case, the radius of the spheres is denoted as $d_{par}/2$, while the radius and length of the cylinder are R and d_{par}, respectively, with R being set to $0.525d_{par}$ to achieve a porosity of 0.4. Here, we define the particle diameter, d_{par}, as 16 mm. It should be noted that the size of d_{par} does not influence the heat transfer due to the fixed porosity. The spherical walls are maintained at a constant high temperature of 333 K, while the inlet gas is at a cooler temperature of 273.15 K. The Reynolds number and Nusselt number for the packed beds are defined as

$$Re = \rho_g|\langle\mathbf{v_g}\rangle|d_{par}/\mu_g \qquad Nu = h_s d_{par}/k_g \qquad (21)$$

where the interstitial heat transfer coefficient between the spheres and gas, denoted as h_s (h_v/A_s), plays a crucial role. Here, A_s, the specific surface area, is defined as $6\varepsilon_s/d_{par}$, and h_v is derived from Eq. (1).
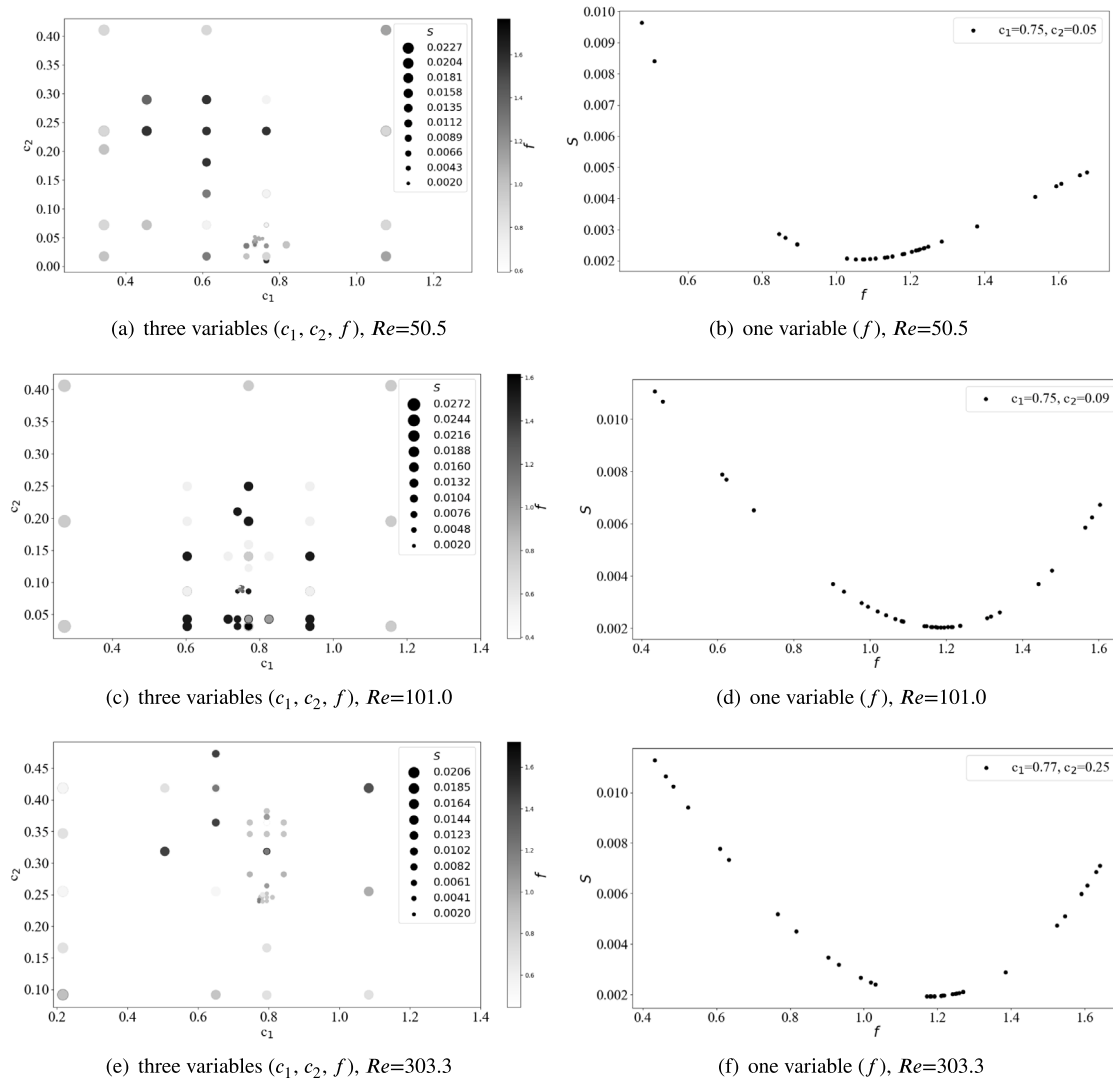
(a) three variables (c_1, c_2, f), Re=50.5

(b) one variable (f), Re=50.5

(c) three variables (c_1, c_2, f), Re=101.0

(d) one variable (f), Re=101.0

(e) three variables (c_1, c_2, f), Re=303.3

(f) one variable (f), Re=303.3

Fig. 32. The influence of the three variables c_1, c_2, f on the error S.

According to the fitting of experimental data, Wakao proposed the following correlation between the Nusselt and the Reynolds numbers [51],

$$Nu = 2 + 1.1 Re^{0.6} Pr^{1/3} \tag{22}$$

Fig. 31 presents a comparison of the Nusselt number variation as a function of the Reynolds number between our simulation and the Wakao equation. The Nusselt number outcomes from this research, as formulated in Eq. (21), match well with the Wakao equation [51], particularly for Reynolds numbers below 30. The relative error across the entire calculation range remains under 5%.

Appendix C. Optimization results at different Reynolds numbers

In this appendix, the optimization results at three different Reynolds numbers using the NL2SOL algorithm in the Dakota software were presented. Fig. 32 showcases the optimization outcomes: the left side displays the effects of three variables (c_1, c_2 and f) on the error S, while the right side focuses on the impact of f alone on S. The process begins by optimizing c_1, and c_2 with all three variables considered. Once c_1, and c_2 are set, f is optimized as a single variable. For the first case at $Re = 50.5$, when S is below 0.002, the optimized values of c_1, and c_2 are around 0.75 and 0.05, respectively, with f ranging from 0.7 to 1.7. Fixing c_1 at 0.75 and c_2 at 0.05, and varying f alone, the minimum error S is obtained at $f = 1.1$, with an uncertainty of $\pm 4\%$, as shown in Fig. 32(b). In the second case ($Re = 101.0$), the optimized values are $c_1 = 0.75$, $c_2 = 0.09$, and $f = 1.2$. For the third case ($Re = 303.3$), the values are $c_1 = 0.77$, $c_2 = 0.25$, and $f = 1.2$.

References

[1] Zhang H, Baeyens J, Degrève J, Cacères G. Concentrated solar power plants: Review and design methodology. Renew Sustain Energy Rev 2013;22:466–81. http://dx.doi.org/10.1016/j.rser.2013.01.032.

[2] O'Sullivan M, Yeh A, Mannington W. Renewability of geothermal resources. Geothermics 2010;39(4):314–20. http://dx.doi.org/10.1016/j.geothermics.2010.09.003.

[3] Edwards J, Bindra H, Sabharwall P. Exergy analysis of thermal energy storage options with nuclear power plants. Ann Nucl Energy 2016;96:104–11. http://dx.doi.org/10.1016/j.anucene.2016.06.005.

[4] Miró L, Brückner S, Cabeza LF. Mapping and discussing Industrial Waste Heat (IWH) potentials for different countries. Renew Sustain Energy Rev 2015;51:847–55. http://dx.doi.org/10.1016/j.rser.2015.06.035.

[5] Yang Y, Pan R, Shuai Y. Investigation of the effect of alumina porous media on the polyethylene waste pyrolysis with continuous feed. Fuel 2024;361:130734. http://dx.doi.org/10.1016/j.fuel.2023.130734.

[6] Alva G, Lin Y, Fang G. An overview of thermal energy storage systems. Energy 2018;144:341–78. http://dx.doi.org/10.1016/j.energy.2017.12.037.

[7] Esence T, Bruch A, Molina S, Stutz B, Fourmigué J-F. A review on experience feedback and numerical modeling of packed-bed thermal energy storage systems. Sol Energyy 2017;153:628–54. http://dx.doi.org/10.1016/j.solener.2017.03.032.

[8] Chen L, He A, Zhao J, Kang Q, Li Z-Y, Carmeliet J, et al. Pore-scale modeling of complex transport phenomena in porous media. Prog Energy Combust Sci 2022;88:100968. http://dx.doi.org/10.1016/j.pecs.2021.100968.

[9] Prat M. Recent advances in pore-scale models for drying of porous media. Chem Eng J 2002;86(1):153–64. http://dx.doi.org/10.1016/S1385-8947(01)00283-2.

[10] Parmigiani A, Huber C, Bachmann O, Chopard B. Pore-scale mass and reactant transport in multiphase porous media flows. J Fluid Mech 2011;686:40–76. http://dx.doi.org/10.1017/jfm.2011.268.

[11] Quintard M, Kaviany M, Whitaker S. Two-medium treatment of heat transfer in porous media: numerical results for effective properties. Adv Water Resour 1997;20(2):77–94. http://dx.doi.org/10.1016/S0309-1708(96)00024-3.

[12] Pan R, Wu Y, Guene Lougou B, Shuai Y, Debenest G. Numerical study on waste polyethylene pyrolysis driven by self-sustaining smoldering. Sci China Technol Sci 2023;1–12. http://dx.doi.org/10.1007/s11431-023-2549-3.

[13] Mikhailenko SA, Sheremet MA. Impacts of rotation and local element of variable heat generation on convective heat transfer in a partially porous cavity using local thermal non-equilibrium model. Int J Therm Sci 2020;155:106427. http://dx.doi.org/10.1016/j.ijthermalsci.2020.106427.

[14] Niu Q, Zhang C. Permeability prediction in rocks experiencing mineral precipitation and dissolution: A numerical study. Water Resour Res 2019;55(4):3107–21. http://dx.doi.org/10.1029/2018WR024174.

[15] Yazdanpanah F. Permeability of bulk wood pellets with respect to airflow [Ph.D. thesis], University of British Columbia; 2009.

[16] Martínez-Mendoza LC, Sánchez-Silva F, Martínez-Mendoza EF, Cruz-Maya JA. Numerical study of fluid flow at pore scale in packed bed of spheres and grains to obtain the REV. CR Mec 2020;348(8–9):769–79. http://dx.doi.org/10.5802/crmeca.62.

[17] Faridkhou A, Hamidipour M, çal Larachi F. Hydrodynamics of gas–liquid micro-fixed beds – measurement approaches and technical challenges. Chem Eng J 2013;223:425–35. http://dx.doi.org/10.1016/j.cej.2013.03.014.

[18] Pozzobon V, Colin J, Perre P. Hydrodynamics of a packed bed of non-spherical polydisperse particles: A fully virtual approach validated by experiments. Chem Eng J 2018;354:126–36. http://dx.doi.org/10.1016/j.cej.2018.07.214.

[19] Dixon AG. Correlations for wall and particle shape effects on fixed bed bulk voidage. Can J Chem Eng 1988;66(5):705–8. http://dx.doi.org/10.1002/cjce.5450660501.

[20] Wakao N, Kaguei S, Funazkri T. Effect of fluid dispersion coefficients on particle-to-fluid heat transfer coefficients in packed beds: Correlation of nusselt numbers. Chem Eng Sci 1979;34(3):325–36. http://dx.doi.org/10.1016/0009-2509(79)85064-2.

[21] Wakao N, Kaguei S. Heat and mass transfer in packed beds Gordon and breach science publications. New York; 1982.

[22] Augier F, Idoux F, Delenne J-Y. Numerical simulations of transfer and transport properties inside packed beds of spherical particles. Chem Eng Sci 2010;65(3):1055–64. http://dx.doi.org/10.1016/j.ces.2009.09.059.

[23] Dorai F, Teixeira CM, Rolland M, Climent E, Marcoux M, Wachs A. Fully resolved simulations of the flow through a packed bed of cylinders: Effect of size distribution. Chem Eng Sci 2015;129:180–92. http://dx.doi.org/10.1016/j.ces.2015.01.070.

[24] Ferguson JC, Panerai F, Borner A, Mansour NN. PuMA: The porous microstructure analysis software. SoftwareX 2018;7:81–7. http://dx.doi.org/10.1016/j.softx.2018.03.001.

[25] Sassanis V, Gamet L, Rolland M, Ma R, Pozzobon V. Numerical determination of the volumetric heat transfer coefficient in fixed beds of wood chips. Chem Eng J 2021;417:128009. http://dx.doi.org/10.1016/j.cej.2020.128009.

[26] Nakayama A, Kuwahara F, Umemoto T, Hayashi T. Heat and fluid flow within an anisotropic porous medium . J Heat Transf 2002;124(4):746–53. http://dx.doi.org/10.1115/1.1481355.

[27] Teruel FE, Díaz L. Calculation of the interfacial heat transfer coefficient in porous media employing numerical simulations. Int J Heat Mass Transfer 2013;60:406–12. http://dx.doi.org/10.1016/j.ijheatmasstransfer.2012.12.022.

[28] Nie Z, Lin Y, Tong Q. Numerical investigation of pressure drop and heat transfer through open cell foams with 3D laguerre-voronoi model. Int J Heat Mass Transfer 2017;113:819–39. http://dx.doi.org/10.1016/j.ijheatmasstransfer.2017.05.119.

[29] Yang J, Wu J, Zhou L, Wang Q. Computational study of fluid flow and heat transfer in composite packed beds of spheres with low tube to particle diameter ratio. Nucl Eng Des 2016;300:85–96. http://dx.doi.org/10.1016/j.nucengdes.2015.10.030.

[30] Scandelli H, Ahmadi-Senichault A, Levet C, Lachaud J. Computation of the permeability tensor of non-periodic anisotropic porous media from 3D images. Transp Porous Media 2022;142(3):669–97. http://dx.doi.org/10.1007/s11242-022-01766-8.

[31] Al-Sumaily GF, Hussen HM, Thompson MC. Validation of thermal equilibrium assumption in free convection flow over a cylinder embedded in a packed bed. Int Commun Heat Mass Transfer 2014;58:184–92. http://dx.doi.org/10.1016/j.icheatmasstransfer.2014.08.039.

[32] Liu S, Ahmadi-Senichault A, Levet C, Lachaud J. Experimental investigation on the validity of the local thermal equilibrium assumption in ablative-material response models. Aerosp Sci Technol 2023;141:108516. http://dx.doi.org/10.1016/j.ast.2023.108516.

[33] Quintard M, Whitaker S. One- and two-equation models for transient diffusion processes in two-phase systems. In: Advances in heat transfer, vol. 23, 1993, p. 369–464. http://dx.doi.org/10.1016/S0065-2717(08)70009-1.

[34] Yang K, Vafai K. Transient aspects of heat flux bifurcation in porous media: An exact solution. J Heat Transf 2011;133(5). http://dx.doi.org/10.1115/1.4003047.

[35] Kaviany M. Principles of heat transfer in porous media. Springer Science & Business Media; 2012.

[36] Kuwahara F, Shirota M, Nakayama A. A numerical study of interfacial convective heat transfer coefficient in two-energy equation model for convection in porous media. Int J Heat Mass Transfer 2001;44(6):1153–9. http://dx.doi.org/10.1016/S0017-9310(00)00166-6.

[37] Kloss C, Goniva C. LIGGGHTS – open source discrete element simulations of granular materials based on lammps. In: Supplemental proceedings. John Wiley & Sons, Ltd; 2011, p. 781–8. http://dx.doi.org/10.1002/9781118062142.ch94.

[38] Falco S, De Cola F, Petrinic N. A method for the generation of 3D representative models of granular based materials. Internat J Numer Methods Engrg 2017;112(4):338–59. http://dx.doi.org/10.1002/nme.5521.

[39] Halkarni SS, Sridharan A, Prabhu S. Estimation of volumetric heat transfer coefficient in randomly packed beds of uniform sized spheres with water as working medium. Int J Therm Sci 2016;110:340–55. http://dx.doi.org/10.1016/j.ijthermalsci.2016.07.012.

[40] Mueller GE. Radial void fraction distributions in randomly packed fixed beds of uniformly sized spheres in cylindrical containers. Powder Technol 1992;72(3):269–75. http://dx.doi.org/10.1016/0032-5910(92)80045-X.

[41] Ahrens J, Geveci B, Law C. 36-Paraview: An end-user tool for large-data visualization. In: The visualization handbook, Citeseer; 2005, p. 717–31. http://dx.doi.org/10.1016/B978-012387582-2/50038-1.

[42] Chen JC, Churchill SW. Radiant heat transfer in packed beds. AIChE J 1963;9(1):35–41.

[43] Nemec D, Levec J. Flow through packed bed reactors: 1. Single-phase flow. Chem Eng Sci 2005;60(24):6947–57. http://dx.doi.org/10.1016/j.ces.2005.05.068.

[44] Quintard M. Introduction to heat and mass transport in porous media. In: Porous media interaction with high temperature and high speed flows, Rhode Saint Genese, Belgium: Von Karman Institute for Fluid Dynamics; 2015.

[45] Lachaud J, Mansour NN. Porous-material analysis toolbox based on OpenFOAM and applications. J Thermophys Heat Transfer 2014;28(2):191–202. http://dx.doi.org/10.2514/1.T4262.

[46] Weller HG, Tabor G, Jasak H, Fureby C. A tensorial approach to computational continuum mechanics using object-oriented techniques. Comput Phys 1998;12(6):620–31. http://dx.doi.org/10.1063/1.168744.

[47] Wang W, He X, Shuai Y, Qiu J, Hou Y, Pan Q. Experimental study on thermal performance of a novel medium-high temperature packed-bed latent heat storage system containing binary nitrate. Appl Energy 2022;309:118433. http://dx.doi.org/10.1016/j.apenergy.2021.118433.

[48] Liu S, Ahmadi-Senichault A, Levet C, Lachaud J. Development and validation of a local thermal non-equilibrium model for high-temperature thermal energy storage in packed beds. J Energy Storage 2024;78:109957. http://dx.doi.org/10.1016/j.est.2023.109957.

[49] McBride BJ, Gordon S, Reno MA. Thermodynamic data for fifty reference elements. NASA TP-3287-REV1, Glenn Research Center, Cleveland, Ohio; 2001.

[50] Jasak H, Jemcov A, Tukovic Z, et al. OpenFOAM: A C++ library for complex physics simulations. In: International workshop on coupled methods in numerical dynamics, vol. 1000, IUC Dubrovnik Croatia; 2007, p. 1–20.

[51] Wakao N, Kaguei S, Nagai H. Effective diffusion coefficients for fluid species reacting with first order kinetics in packed bed reactors and discussion on evaluation of catalyst effectiveness factors. Chem Eng Sci 1978;33(2):183–7. http://dx.doi.org/10.1016/0009-2509(78)85052-0.

[52] Montillet A. Flow through a finite packed bed of spheres: A note on the limit of applicability of the Forchheimer-type equation . J Fluids Eng 2004;126(1):139–43. http://dx.doi.org/10.1115/1.1637928.

[53] Mei C, Auriault J-L. The effect of weak inertia on flow through a porous medium. J Fluid Mech 1991;222:647–63. http://dx.doi.org/10.1017/S0022112091001258.

[54] Whitaker S. The method of volume averaging, vol. 13, Springer Science & Business Media; 2013.

[55] Lasseux D, Abbasian Arani AA, Ahmadi A. On the stationary macroscopic inertial effects for one phase flow in ordered and disordered porous media. Phys Fluids 2011;23(7):073103. http://dx.doi.org/10.1063/1.3615514.

[56] Ergun S. Fluid flow through packed columns. Chem Eng Prog 1952;48(2):89–94.

[57] Lachaud J, Scoggins JB, Magin TE, Meyer MG, Mansour NN. A generic local thermal equilibrium model for porous reactive materials submitted to high temperatures. Int J Heat Mass Transfer 2017;108:1406–17. http://dx.doi.org/10.1016/j.ijheatmasstransfer.2016.11.067.

[58] Amao AM. Mathematical model for Darcy forchheimer flow with applications to well performance analysis [Ph.D. thesis], 2007.

[59] Lachaud J, Scoggins JB, Magin TE, Meyer MG, Mansour NN. A generic local thermal equilibrium model for porous reactive materials submitted to high temperatures. Int J Heat Mass Transf 2017;108:1406–17. http://dx.doi.org/10.1016/j.ijheatmasstransfer.2016.11.067.

[60] lin Xia X, Chen X, Sun C, huan Li Z, Liu B. Experiment on the convective heat transfer from airflow to skeleton in open-cell porous foams. Int J Heat Mass Transf 2017;106:83–90. http://dx.doi.org/10.1016/j.ijheatmasstransfer.2016.10.053.

[61] Adams BM, Bohnhoff WJ, Dalbey K, Ebeida MS, Eddy JP, Eldred MS, et al. Dakota, a multilevel parallel object-oriented framework for design optimization, parameter estimation, uncertainty quantification, and sensitivity analysis: version 6.15 user's manual. Sandia Technical Report SAND2020-12495, 2021.

[62] Dennis Jr JE, Gay DM, Walsh RE. An adaptive nonlinear least-squares algorithm. ACM Trans Math Software 1981;7(3):348–68.

[63] Noël E, Teixeira D, Preux G. Modelling of gas-solid heat transfer and pressure drop in a rock-packed bed using pore-scale simulations. Int J Heat Mass Transfer 2023;214:124432. http://dx.doi.org/10.1016/j.ijheatmasstransfer.2023.124432.

[64] Chhabra R. Fluid flow and heat transfer from circular and noncircular cylinders submerged in non-Newtonian liquids. In: Cho YI, Greene GA, editors. In: Advances in heat transfer, vol. 43, Elsevier; 2011, p. 289–417. http://dx.doi.org/10.1016/B978-0-12-381529-3.00004-9.

[65] Qu Y, Wang L, Lin X, Chen H, Zhang S, Ling H, et al. Mixed convective heat transfer characteristics and mechanisms in structured packed beds. Particuology 2023;82:122–33. http://dx.doi.org/10.1016/j.partic.2023.01.014.

[66] Saghir M, Jiang C, Yan Y, Khawaja M, Pan S, Chacha M. 9 - Thermodiffusion in porous media. In: Ingham D, Pop I, editors. Transport phenomena in porous media III. Oxford: Pergamon; 2005, p. 227–60. http://dx.doi.org/10.1016/B978-008044490-1/50013-2.

[67] Chakkingal M, de Geus J, Kenjereš S, Ataei-Dadavi I, Tummers M, Kleijn CR. Assisting and opposing mixed convection with conjugate heat transfer in a differentially heated cavity filled with coarse-grained porous media. Int Commun Heat Mass 2020;111:104457. http://dx.doi.org/10.1016/j.icheatmasstransfer.2019.104457.

[68] Linsong J, Ping W, Antonio F. Multi-scale simulation of turbulence and heat transfer characteristics in randomly packed beds. Powder Technol 2021;377:29–40. http://dx.doi.org/10.1016/j.powtec.2020.08.077.